[American Journal of Science, Vol. 305, November, 2005, P. 919–956]

QUANTITATIVE INTERPRETATION OF pH DISTRIBUTIONS IN AQUATIC SEDIMENTS: A REACTION-TRANSPORT MODELING APPROACH

PARISA JOURABCHI†, PHILIPPE VAN CAPPELLEN, and PIERRE REGNIER

Department of Earth Sciences, Geochemistry, Utrecht University,
P.O. Box 80021, 3508 TA Utrecht, The Netherlands

ABSTRACT. Despite its status of master variable, there have been relatively few attempts to quantitatively predict the distributions of pH in biogeochemical reactive transport systems. Here, we propose a theoretical approach for calculating the vertical pore water profiles of pH and the rates of proton production and consumption in aquatic sediments. In this approach, the stoichiometric coefficients of species that participate in acid-base equilibrium reactions are treated as unknown variables in the biogeochemical reaction network. The mixed kinetic-equilibrium reaction system results in a set of coupled differential and algebraic equations and is solved using a new numerical solver. The diagnostic capabilities of the model are illustrated for depositional conditions representative of those encountered on the continental shelf. The early diagenetic reaction network includes the major microbial degradation pathways of organic matter and associated secondary redox reactions, mineral precipitation and dissolution processes, and homogeneous acid-base reactions. The resulting pH profile in this baseline simulation exhibits a sharp decrease below the sediment-water interface, followed by an increase with depth and again a decrease. The features of the pH profile are explained in terms of the production and consumption of protons by the various biogeochemical processes. Secondary oxygenation reactions are the principal proton producers within the oxic zone, while reduction of iron and manganese oxyhydroxides are primarily responsible for the reversal in the pH gradient in the suboxic zone. Proton production in the zone of sulfate reduction outweighs alkalinity production, maintaining the undersaturation of the pore waters with respect to calcite. Integrated over the entire depth of early diagenesis, dissolution of $CaCO_3$ is the main sink for protons. Variations in the reaction rate order and rate constant for $CaCO_3$ dissolution do not fundamentally alter the shape of the pH profile. An entirely different shape is obtained, however, when the pore waters are assumed to remain in thermodynamic equilibrium with calcite at all depths. Pore water (bio)irrigation decreases the amplitude of pH changes in the sediment and may modify the shape of the pH profile.

INTRODUCTION

The dissolved hydrogen ion concentration is considered a master variable in aquatic (bio)geochemistry (Stumm and Morgan, 1996). The pH of the aqueous medium influences the occurrence and biochemical activity of organisms, the saturation state with respect to most reactive mineral phases, and the adsorption of soluble species. In turn, the spatial and temporal distribution of pH in a given environment may provide information on the biogeochemical reactivity and buffering capacity of the system.

The unique status of the aqueous hydrogen ion, $H^+(aq)$, in the biogeochemistry of aquatic sediments has been reviewed in detail by Boudreau and Canfield (1993). Measured pore water pH profiles exhibit distinct features, which can be related to bottom water chemistry, solid sediment composition, and redox reactions associated with the degradation of organic matter. In the majority of studies, however, pH profiles are only used as qualitative support for the interpretation of early diagenetic data sets, or they are imposed *a priori* when performing saturation state calculations (Hales and

†Corresponding author: Parisa Jourabchi, parisa@geo.uu.nl

Table 1

Comparison of existing reactive transport models (RTMs) of early diagenesis that consider both kinetic and equilibrium reactions

Study/ model	Numerical scheme	Steady state solution	Transport
This study/ BRNS-global	global	direct	species
Katsev and others (unpublished data)/ LSSE	global	TD	species
Hales (2003)	OS	direct	species
Luff and others (2003) / C.CANDI	global	TD	species & components
Meysman and others (2003) /MEDIA	global	TD	species
Archer and others (2002) / Muds	global	direct	components
Regnier and others (2002) / BRNS-OS	OS	TD	species
Adler and others (2001) / CoTReM	OS	TD	species
Hensen and others (1997) / CoTAM	OS	TD	species
Jahnke and others (1997)	global	TD	species
Boudreau (1996) / CANDI	global	TD	components
Van Cappellen and Wang (1995) /SteadySed	global	direct	components
Archer and others (1989)	global	TD (solids) direct (solutes)	species

The numerical scheme is noted as either global or operator splitting (OS). In the first case, at every time step or iteration, the concentrations of all species are solved for simultaneously at all spatial nodes. In the second case, at every time step or iteration, transport (of every species or component) and reaction (at every spatial node) calculations are performed in sequence.

The method of obtaining steady state solutions is divided into two categories. In the time-dependent (TD) approach the transient solution is allowed to evolve until it meets a pre-defined criterion indicating no further change in the species concentrations with time. In the direct solution the net rate of change of each species concentrations is set to zero, and the set of coupled ordinary differential equations representing mass conservation are solved directly.

The RTMs may be based on mass balance equations written either for individual chemical species, or for components (linear combinations of subsets of chemical species), thereby reducing the number of state variables. In the latter approach, the transport properties of each component are calculated as the weighted average of the properties of individual species comprising the component. Three models (Hales, 2003; LSSE; MEDIA) use components for mass balance equations, yet compute the concentration and gradient of individual species in calculating the mass flux of the component.

others, 1994; Cai and others, 1995; Reimers and others, 1996; Carman and Rahm, 1997; Hales and Emerson, 1997a; Hensen and others, 1997; Luff and others, 2000; Thamdrup and others, 2000; Adler and others, 2001; Wijsman and others, 2002; Müller and others, 2003; Forja and others, 2004).

The lack of systematic quantitative treatment of pH distributions in early diagenetic studies partially reflects the highly complex reaction network controlling the acid-base properties of pore waters (for example, Boudreau and Canfield, 1988). With the exception of water, H^+ (and OH^-) ions participate in more chemical reactions than any other species. Even in a closed-system, the calculation of pH due to biogeochemical reactions is not a simple task (Ben-Yaakov, 1973). The difficulty is compounded, by the coupling of reaction and transport processes in sediments. Kulik and others (2000) and Wijsman and others (2002) have reviewed the challenges of accurate and efficient computation of pH distributions in reactive transport models, while Luff and others (2001) provide a detailed comparison of three methods for their calculation: alkalinity conservation, charge balance, and the "advancement approach".

A limited number of early diagenetic reactive transport codes include an explicit calculation of pore water pH (see table 1, for a summary). In some models, a linear combination of a subset of dissolved species such as alkalinity or total dissolved

inorganic carbon are transported as components, to which weighted average transport properties are assigned (for example, STEADYSED and CANDI, table 1). In other models (for example, C. CANDI, MEDIA, and BRNS, table 1), transport fluxes are calculated for all individual species (for example, HCO_3^-, CO_3^{2-} and $CO_2 \equiv CO_2 + H_2CO_3$). Using a simple example, Luff and others (2001) demonstrate that transporting individual protolytic species participating in equilibrium reactions, rather than transporting components, can lead to non-negligible differences in species distributions among reactive transport models, unless the system is strongly dominated by calcium carbonate dissolution. Even in the latter case, the authors show that there can be significant differences in the calculated solute fluxes across the sediment water interface.

Because pH distributions are intimately linked to all major biogeochemical reaction processes in sediments, and because they can be measured accurately and with high vertical resolution (for example: Fisher and Matisoff, 1981; Archer and others, 1989; Cai and Reimers, 1993; Cai and others, 1995; Hales and Emerson, 1996; Reimers and others, 1996; Komada and others, 1998; Wenzhöfer and others, 2001), they possess unequalled diagnostic capabilities. To unlock these capabilities, however, it is necessary to combine measured pH profiles with a quantitative description of the production and consumption of H^+(aq) in sediments. In this paper, we address the theoretical challenges of modeling reactive transport in mixed kinetic-equilibrium reaction systems dominated by molecular diffusion of the solutes, and propose a general approach to include H^+(aq) in multi-species early diagenetic models. The added value of a process-based interpretation of pore water pH profiles is illustrated by performing steady state simulations of a representative continental shelf sediment.

THEORY

Mass Conservation

Reactive transport in sediments is described by the general diagenetic equation for mass conservation of solid and dissolved species (Berner, 1980). Using C_k to represent the concentration of a solid or dissolved species, this equation can be written as:

$$\frac{\partial(\xi_k C_k)}{\partial t} = -\nabla \cdot F_k + \sum_i s_k^i R^i + \alpha_k \xi_k (C_{k0} - C_k), \tag{1}$$

where t is time, F_k is the sum of all advective and diffusive fluxes of the k^{th} species, s_k^i is the stoichiometric coefficient of species k in the kinetically controlled reaction i, with rate R^i (expressed per unit of total volume of sediment), and ξ_k is the volume fraction in which the concentration of species k is defined. For example, in a two phase (solid/solute) system, the concentration of a dissolved species is usually given in units of mass per unit volume of pore water, hence, ξ_k = porosity (ϕ). Likewise, for a solid species, whose concentration is expressed per unit volume of solid sediment, $\xi_k = (1 - \phi)$. Pore water irrigation is included in the mass conservation equation as a source or sink function analogous to a kinetic rate. It is calculated as the product of the irrigation intensity, α_k ($\alpha_k = 0$ for all solids) and the difference in concentration of species k relative to the concentration at the sediment-water interface (SWI), C_{k0}.

In the absence of externally impressed flow, the advective and diffusive fluxes in equation (1) arise from sediment burial (rate = ω_k), biodiffusional mixing or bioturbation (coefficient = D_b), and molecular diffusion (coefficient = D_k). While we assume that D_b is the same for all species, the burial rate of solids may differ from that of the

Table 2

Species and stoichiometric coefficients in a simple system involving only oxic respiration of organic matter (CH_2O) as kinetic reaction process

Species # k	Species	s_k^1
1	CH_2O	-1
2	O_2	-1
3	CO_2	Variable
4	HCO_3^-	Variable
5	CO_3^{2-}	Variable
6	H^+	Variable
7	OH^-	Variable
8	H_2O	Variable

dissolved species, for instance due to sediment compaction. By expanding the flux term in equation (1) in one-dimension, we obtain

$$\frac{\partial(\xi_k C_k)}{\partial t} = -\frac{\partial(\xi_k \omega_k C_k)}{\partial x} + \frac{\partial}{\partial x}\left(D_b \varphi \frac{\partial(\xi_k C_k)}{\partial x} + D_b(1-\varphi)\xi_k \frac{\partial C_k}{\partial x} + D_k \xi_k \frac{\partial C_k}{\partial x}\right) + \sum_i s_k^i R^i + \alpha_k(C_{k0} - C_k), \quad (2)$$

where x is depth into the sediment ($x = 0$ at the SWI) and $D_k = 0$ for all solid species. Equation (2) is based on the general diagenetic equation presented by Berner (1980), where the parameter, φ, defines the mixing model used in describing bioturbation ($0 < \varphi < 1$). The end member mixing models are (1) interphase mixing with $\varphi = 1$, in which the solids and pore waters are assumed to intermix in the bioturbation process, hence altering the depth dependence of porosity, and (2) intraphase mixing with $\varphi = 0$, in which sediment porosity is assumed to be unaffected (Boudreau, 1986; Mulsow and others, 1998). In this paper, the intraphase mixing model is used.

In general, the rate of a kinetically controlled reaction (or 'slow' reaction) is a function of a subset of the species concentrations. The full mathematical description of the reactive transport system thus requires the solution of a set of coupled partial differential equations in the form of equation (2). In the absence of fast reversible reactions, and when the stoichiometric coefficients, s_k^i, and transport properties of each species are well defined, the number of unknown state variables (C_k) is equal to the number of partial differential equations. The latter can be solved numerically with appropriately specified initial and boundary conditions.

However, due to 'fast' reversible reactions, which algebraically relate some of the species concentrations through mass action laws, it is not possible to uniquely specify, *a priori,* the stoichiometric coefficients of these species involved in the kinetic reactions, at all points in time and space. To illustrate with a simple example, consider the bacterially mediated oxidation of organic matter (represented by the simplified formula CH_2O) by O_2 in pure water with no gas exchange. The state variables are CH_2O, O_2, the three carbonate species (CO_2, HCO_3^-, and CO_3^{2-}), protons (H^+), hydroxyls (OH^-), and H_2O (table 2). Although the stoichiometric coefficient of total dissolved inorganic carbon, *DIC* can be defined exactly,

$$CH_2O + O_2 \rightarrow DIC + s_6^1 H^+ + s_7^1 OH^- + s_8^1 H_2O, \qquad R^1 \quad (3a)$$

those of the protons, hydroxyls, individual carbonate species, and H_2O depend upon the speciation of *DIC* and water as governed by the equilibria

$$CO_2 \leftrightarrow H^+ + HCO_3^-$$

$$HCO_3^- \leftrightarrow H^+ + CO_3^{2-},$$

$$H_2O \leftrightarrow H^+ + OH^- \tag{3b}$$

and their corresponding mass action laws,

$$K_1^* = \frac{[H^+][HCO_3^-]}{[CO_2]} = \frac{C_6 C_4}{C_3}$$

$$K_2^* = \frac{[H^+][CO_3^{2-}]}{[HCO_3^-]} = \frac{C_6 C_5}{C_4}. \tag{4}$$

$$K_3^* = \frac{[H^+][OH^-]}{[H_2O]} = \frac{C_6 C_7}{C_8}$$

The dissociation constants K_1^*, K_2^*, and K_3^* of carbonic acid, bicarbonate, and water, used in the mass action laws (eqs 4) correspond to apparent (or otherwise referred to as stoichiometric) constants based on a total concentration scale (Pilson, 1998). They may therefore vary with temperature, pressure, ionic strength and relative composition of the solution.

Taking into account all possible species, reaction (3a) can now be rewritten as

$$s_1^1 CH_2O + s_2^1 O_2 \rightarrow s_3^1 CO_2 + s_4^1 HCO_3^- + s_5^1 CO_3^{2-} + s_6^1 H^+ + s_7^1 OH^- + s_8^1 H_2O, \tag{5}$$

where the stoichiometric coefficients of 6 of the 8 species are additional unknowns in the system (table 2). Omitting the concentration of H_2O as an explicit state variable (Morel and Hering, 1993), the solution of the system of 7 partial differential equations expressing mass conservation of the 7 unknown concentrations, $C_1 - C_7$, requires prior knowledge of s_3^1, s_4^1, s_5^1, s_6^1 and s_7^1. However, fulfilling the equilibrium conditions gives rise to three additional constraints through the mass action laws (eqs 4), which together with conservation of total dissolved inorganic carbon and charge balance, close the full mathematical description of the system of 12 unknowns (7 species and 5 stoichiometric coefficients) and 12 linearly independent equations (7 partial differential and 5 algebraic equations).

Stoichiometric Coefficients

The following is a derivation of expressions for the stoichiometric coefficients of protolytic species in an example seawater system, considering the acid-base equilibria for borates, sulfides, and carbonates. It should be noted that the approach based on stoichiometric coefficients can, in principle, be extended to other equilibrium reactions, including heterogeneous reactions such as adsorption or mineral solubility reactions. The common variable in all equilibrium conditions considered here is the total proton concentration $[H^+]$, which includes not only the proton or hydronium ion concentration, but also the concentrations of HSO_4^- and HF in solution, in accordance with the seawater scale for pH (Pilson, 1998).

To calculate the rate of production or consumption of protons by a given kinetically controlled reaction i, with rate R^i, we define the stoichiometric coefficients of total dissolved inorganic carbon (T_C), total dissolved sulfide (T_S), total dissolved borate (T_B), and total alkalinity (T_A) to be t_c^i, t_s^i, t_b^i, and t_a^i, respectively, such that

$$\left.\frac{dT_C}{dt}\right|_i = t_c^i R^i$$
$$\left.\frac{dT_S}{dt}\right|_i = t_s^i R^i$$
$$\left.\frac{dT_B}{dt}\right|_i = t_b^i R^i \quad . \tag{6}$$
$$\left.\frac{dT_A}{dt}\right|_i = t_a^i R^i$$

These stoichiometric coefficients (t_c^i, t_s^i, t_b^i, and t_a^i) are uniquely defined for each kinetic reaction, i, and remain constant at all points in time and space. It is important to note that the time derivatives in equation (6) refer only to rates of change due to kinetic reactions. In the following, we assume that there are no reactions affecting the concentration of total borates and, thus, $t_b^i = 0$ for all i.

Using the total proton concentration as the master variable, each equilibrium species concentration can be written as a fraction of the total component concentration

$$[HCO_3^-] = \chi_1 T_C$$
$$[CO_3^{2-}] = \chi_2 T_C$$
$$[CO_2] = \chi_3 T_C$$
$$[HS^-] = \sigma_1 T_S, \tag{7}$$
$$[H_2S] = \sigma_2 T_S$$
$$[B(OH)_4^-] = \beta_1 T_B$$
$$[B(OH)_3] = \beta_2 T_B$$

where the fractions are

$$\chi_1 \equiv \frac{K_1^* [H^+]}{[H^+]^2 + K_1^*[H^+] + K_1^* K_2^*}$$
$$\chi_2 \equiv \chi_1 \frac{K_2^*}{[H^+]}$$
$$\chi_3 \equiv 1 - \chi_1 - \chi_2$$
$$\sigma_1 \equiv \frac{K_4^*}{K_4^* + [H^+]} \quad . \tag{8}$$
$$\sigma_2 \equiv 1 - \sigma_1$$
$$\beta_1 \equiv \frac{K_5^*}{K_5^* + [H^+]}$$
$$\beta_2 \equiv 1 - \beta_1$$

In the above equations, we use the apparent dissociation constants, K_4^* and K_5^*, for the dissociation of H_2S and $B(OH)_3$, respectively. As with K_1^*, K_2^*, and K_3^*, these parameters depend on the pressure, temperature, ionic strength and relative composition of the solution.

From the definition of total alkalinity in our system,

$$T_A = T_C(\chi_1 + 2\chi_2) + T_S\sigma_1 + T_B\beta_1 + \frac{K_3^*}{[H^+]} - [H^+], \tag{9}$$

the rate of alkalinity production by a given kinetic reaction i is derived as

$$\begin{aligned}\left.\frac{dT_A}{dt}\right|_i = \left.\frac{dT_C}{dt}\right|_i (\chi_1 + 2\chi_2) + T_C \frac{\partial(\chi_1 + 2\chi_2)}{\partial[H^+]} \left.\frac{d[H^+]}{dt}\right|_i + \left.\frac{dT_S}{dt}\right|_i \sigma_1 \\ + T_S \frac{\partial\sigma_1}{\partial[H^+]} \left.\frac{d[H^+]}{dt}\right|_i + \left.\frac{dT_B}{dt}\right|_i \beta_1 + T_B \frac{\partial\beta_1}{\partial[H^+]} \left.\frac{d[H^+]}{dt}\right|_i \\ - \frac{K_3^*}{[H^+]^2} \left.\frac{d[H^+]}{dt}\right|_i - \left.\frac{d[H^+]}{dt}\right|_i + \sum_{m=1}^{N_{eq}} \eta_m \left.\frac{dK_m^*}{dt}\right|_i, \end{aligned} \tag{10}$$

which can also be expressed in terms of the instantaneous rates of T_A, T_C, and T_S production (eq 6)

$$\begin{aligned}(t_a^i - t_c^i(\chi_1 + 2\chi_2) - t_s^i\sigma_1)R^i = \\ \left(T_C \frac{\partial(\chi_1 + 2\chi_2)}{\partial[H^+]} + T_S \frac{\partial\sigma_1}{\partial[H^+]} + T_B \frac{\partial\beta_1}{\partial[H^+]} - \frac{K_3^*}{[H^+]^2} - 1\right) \\ \left.\frac{d[H^+]}{dt}\right|_i + \sum_{m=1}^{N_{eq}} \eta_m \left.\frac{dK_m^*}{dt}\right|_i. \end{aligned} \tag{11}$$

The last term on the right hand side (RHS) of equations (10) and (11) represents the rate of change of each of the N_{eq} apparent equilibrium constants, K_m^*, due to changes in the activity coefficients of the solute species (Appendix I).

In systems where the apparent dissociation constants are assumed to be invariant with respect to time and space, the instantaneous rate of proton production/consumption can be solved for explicitly. This assumption allows us to express the instantaneous rate of proton production or consumption due to each kinetically controlled reaction i, as

$$\left.\frac{d[H^+]}{dt}\right|_i = \frac{t_a^i - (\chi_1 + 2\chi_2)t_c^i - t_s^i\sigma_1}{A_1} R^i. \tag{12}$$

where A_1 is defined by

$$A_1 \equiv T_C \frac{\partial\chi_1}{\partial[H^+]} + 2T_C \frac{\partial\chi_2}{\partial[H^+]} + T_S \frac{\partial\sigma_1}{\partial[H^+]} + T_B \frac{\partial\beta_1}{\partial[H^+]} - \frac{K_3}{[H^+]^2} - 1. \tag{13}$$

Thus, the stoichiometric coefficient of protons for each reaction i is

$$s_{H^+}^i = \frac{t_a^i - (\chi_1 + 2\chi_2)t_c^i - t_s^i\sigma_1}{A_1}, \tag{14}$$

Table 3

Description of symbols used in the proposed numerical solution (Numerical Solution section). Arrows and bold font are used to indicate vectors and matrices, respectively. The dimension of all vectors and matrices are provided in square brackets

x	depth into the sediment ($x = 0$ at the SWI)
t	time
N_x	number of spatial nodes in the model domain
N_s	number of species
$C^j_{\ell/k}$	species ℓ/k concentration at node j
$R^{i,j}$	rate of reaction i at node j
α^j_k	irrigation intensity of species k at node j
$s^{i,j}_k$	stoichiometric coefficient of species k in reaction i at node j
R^j_k	total rate (source and sink) of species k at node j
$\vec{C}_k$	concentration vector of species k for all nodes [Nx]
$\vec{R}_k$	total rate vector of species k for all nodes [Nx]
$\boldsymbol{T}_k$	tri-diagonal transport matrix for species k [Nx, Nx]
ξ_k	diagonal volume fraction matrix for species k [Nx, Nx]
Δt	time step
N	number of species times the number of nodes ($NsNx$)
$\boldsymbol{J}^j$	jacobian matrix of total rates with respect to species at node j [Ns, Ns]
$\vec{C}$	concentration vector for all species at all nodes [N]
$\vec{R}$	total rates vector for all species at all nodes [N]
$\boldsymbol{T}$	(diagonal-)block tri-diagonal transport matrix [N, N]
ξ	diagonal volume fraction matrix [N, N]
$\boldsymbol{J}$	block diagonal jacobian matrix [N, N]
$\vec{C}\Big\vert_{eq}$	equilibrium concentration vector of all species at all nodes (see text) [N]
β^j	diagonal Lagrange multiplier matrix at node j [Ns, Ns]
β	Diagonal Lagrange multiplier matrix at all nodes [N, N]
$\boldsymbol{G}$	block tri-diagonal matrix (see fig. 1) [N, N]
$\vec{d}$	vector on the RHS of equation in the global approach (see fig. 1) [N]
$\boldsymbol{G}^j$	diagonal block j of $\boldsymbol{G}$ [Ns, Ns]

which depends on the proton concentration and can be used in conjunction with equations (7) and (8) in order to calculate the stoichiometric coefficients of the remaining protolytic species. The explicit calculation of proton production or consumption rates (eq 12) provides the basis for the quantitative interpretation of the pore water pH distribution in terms of individual reactions.

Numerical Solution

A method for the numerical solution of the Differential-Algebraic Equation (DAE) system is presented in two parts. In the first part, we describe the spatially discretized mass conservation equation for a single species. This equation is then used in the second part to derive a global implicit equation for all species at all nodes in the model domain. A summary of the symbols used in this section is provided in table 3.

Discretized equation for a single species.—For each of the N_s chemical species in the mixed kinetic-equilibrium reaction system, the mass conservation equation (2) is spatially discretized as

$$\frac{\partial(\boldsymbol{\xi}_k \vec{C}_k)}{\partial t} = \boldsymbol{T}_k \vec{C}_k + \vec{R}_k, \tag{15}$$

in which $\boldsymbol{T}_k$ is the N_x by N_x tri-diagonal matrix containing the transport terms and boundary conditions of species k, N_x denoting the number of spatial nodes in the model domain. The vectors $\vec{C}_k$ and $\vec{R}_k$ are each of length N_x. Their respective elements are the concentration of species k and the sum of all sources and sinks affecting species k, respectively, at every node in the model domain. The volume fractions at each node are represented by the diagonal matrix, $\boldsymbol{\xi}_k$, of dimension N_x by N_x. In $\boldsymbol{\xi}_k$, every diagonal entry represents the volume fraction at a specific node in the domain for species k.

The sources and sinks are defined by all the kinetic reaction rates and irrigation intensities, and their corresponding stoichiometric coefficients, affecting species, k, at every node, j, such that every element in vector $\vec{R}_k$ can be represented by

$$R^j_k \equiv \sum_i s^{i,j}_k R^{i,j} + \alpha^j_k \boldsymbol{\xi}^j_k (C_{k0} - C^j_k), \tag{16}$$

where $R^{i,j}$ is the rate of reaction i, as defined in the *Mass Conservation section,* at node j and $s^{i,j}_k$ is the stoichiometric coefficient of the k^{th} species in the i^{th} reaction at node j.

Discretized equation for all species: global implicit scheme.—The spatially discretized reaction-transport equations for all species k result in a set of N_s non-linear equations, each of which has a unique transport matrix $\boldsymbol{T}_k$. The reaction terms couple the set of equations at each node, j, as the rates may depend on more than one species concentration. The set of equations are solved iteratively by using implicit numerical schemes for the transport and reaction terms. The latter is approximated by a first-order Taylor series expansion with respect to each of the species concentrations. Note that $\boldsymbol{T}_k$ may depend on the species concentration through composition-dependent diffusion coefficients (Van Cappellen and Gaillard, 1996).

The Taylor expansion of the total rate terms and the temporal discretization of equation (15) is detailed in Appendix II. The discretized mass conservation equation (II-4) can be recast as

$$(\boldsymbol{\xi} - \boldsymbol{\Delta} t \boldsymbol{T} - \Delta t \boldsymbol{J}\big|^{t_{m+1}}_{old}) \vec{C}\big|^{t_{m+1}}_{new} = \boldsymbol{\xi} \vec{C}\big|^{t_m} - \Delta t \boldsymbol{J}\big|^{t_{m+1}}_{old} \vec{C}\big|^{t_{m+1}}_{old} + \Delta t \vec{R}\big|^{t_{m+1}}_{old}, \tag{17}$$

and solved iteratively for the transient solution. In order to obtain the steady state solution, the rate of change of species concentrations on the left hand side of equation (II-4) is set to zero, and an initial guess for $\vec{C}|_{old}$ is used to calculate $\vec{C}|_{new}$:

$$(\boldsymbol{T} + \boldsymbol{J}|_{old}) \vec{C}|_{new} = \boldsymbol{J}|_{old} \vec{C}|_{old} - \vec{R}|_{old}. \tag{18}$$

Incorporation of equilibrium constraints.—As discussed in the *Mass Conservation* section, solution of equation (17) or (18) requires values for the stoichiometric coefficients, s^i_k, of the species involved in the fast acid-base reactions. Some reactive transport models decouple the computations involving the algebraic equations for the equilibrium constraints, from those involving the differential equations arising from the mass balance of components (for example, Marzal and others, 1994; Van Cappellen and Wang, 1995). In these models, the operator-splitting of the equilibrium and kinetic calculations is combined with a sequential iterative approach to reach convergence of the species concentrations. Here, we have directly implemented the equilibrium constraints in the discretized mass balance equations (that is, equation 17 or 18 for transient or steady state conditions) through the use of stoichiometric coefficients s^i_k.

Prior to each iteration step, the concentration values $\vec{C}|_{old}$ are used to define the conserved quantities corresponding to the equilibrium reactions. In the example described in the *Stoichiometric Coefficients* section, these quantities are T_C, T_S, T_B and T_A. At this point, if necessary, the ionic strength of the solution, the activity coefficients, ionic diffusion coefficients, and the apparent equilibrium constants can be updated using appropriate models (for example, non-ideal effects can be accounted for by ion pairing calculations or Pitzer's equations). An equilibrium speciation module then calculates the corresponding equilibrium concentrations for the subset of species involved in the equilibrium reactions, $\vec{C}|_{eq}$, from which the unknown stoichiometric coefficients, s^i_{eq} to be used in the kinetic reactions are derived.

In the approach outlined above, the stoichiometric coefficient of protons (as defined, for example, by equation (14) in the example of the *Stoichiometric Coefficients* section) and the proton concentration are defined independently of the stoichiometric coefficients of the other equilibrium acid-base species. That is, the mathematical system of algebraic-differential equations is over-determined and one of the equations must be omitted. A natural choice is to eliminate the mass balance equation of the proton itself. The proton (or pH) distribution can then be viewed as the necessary condition for closure of the mixed kinetic-equilibrium reactive transport system. An important advantage of this choice is that it eliminates the uncertainties associated with the deviating diffusion behavior of protons in aqueous solution (for example, Cussler, 1984).

In our global approach, the equilibrium constraints are coupled to the transport and kinetic reactions calculations by introducing a Lagrange multiplier term,

$$\boldsymbol{\beta}(\vec{C}|_{new} - \vec{C}|_{eq}), \tag{19}$$

in equation (17) or (18). For every node in the model domain, the Lagrange multiplier $\boldsymbol{\beta}^j$, is set to the largest transport coefficient in the corresponding diagonal block of matrix $\boldsymbol{T}$. For consistency, $\vec{C}|_{eq}$ is defined as a vector of length N_sN_x, where the entries corresponding to species not involved in the equilibrium reactions are simply assigned their $\vec{C}|_{old}$ values. Following this strategy, $\boldsymbol{\beta}$ is thus defined as a diagonal matrix of the same shape and dimension as $\boldsymbol{\xi}$. This approach is preferred, because it ensures a fast and robust convergence to the solution.

The final equations obtained for the iterative solutions of the transient and steady state cases are then, respectively

$$(\boldsymbol{\xi} - \Delta t\boldsymbol{T} - \Delta t\,\boldsymbol{J}|^{t_{m+1}}_{old} + \Delta t\boldsymbol{\beta})\vec{C}|^{t_{m+1}}_{new} = \boldsymbol{\xi}\vec{C}|^{t_m} - \Delta t\,\boldsymbol{J}|^{t_{m+1}}_{old}\vec{C}|^{t_{m+1}}_{old} + \Delta t\vec{R}|^{t_{m+1}}_{old} + \Delta t\boldsymbol{\beta}\vec{C}|_{eq}, \tag{20}$$

and

$$(\boldsymbol{T} + \boldsymbol{J}|_{old} + \boldsymbol{\beta})\vec{C}|_{new} = \boldsymbol{J}|_{old}\vec{C}|_{old} - \vec{R}|_{old} + \boldsymbol{\beta}\vec{C}|_{eq}. \tag{21}$$

Numerical implementation.—For both transient and steady state solutions, the numerical equation to be solved at each iteration step, assumes the general form

$$\boldsymbol{G}\vec{C}|_{new} = \vec{d}, \tag{22}$$

with $\boldsymbol{G}$ as a sparse, N by N, block tri-diagonal matrix,

$$\boldsymbol{G} = \begin{bmatrix} [\boldsymbol{G}^1] & [\ddots] & & & \\ [\ddots] & [\boldsymbol{G}^2] & \ddots & & \\ & \ddots & \ddots & \ddots & \\ & & \ddots & [\boldsymbol{G}^{N_x-1}] & [\ddots] \\ & & & [\ddots] & [\boldsymbol{G}^{N_x}] \end{bmatrix}, \tag{23}$$

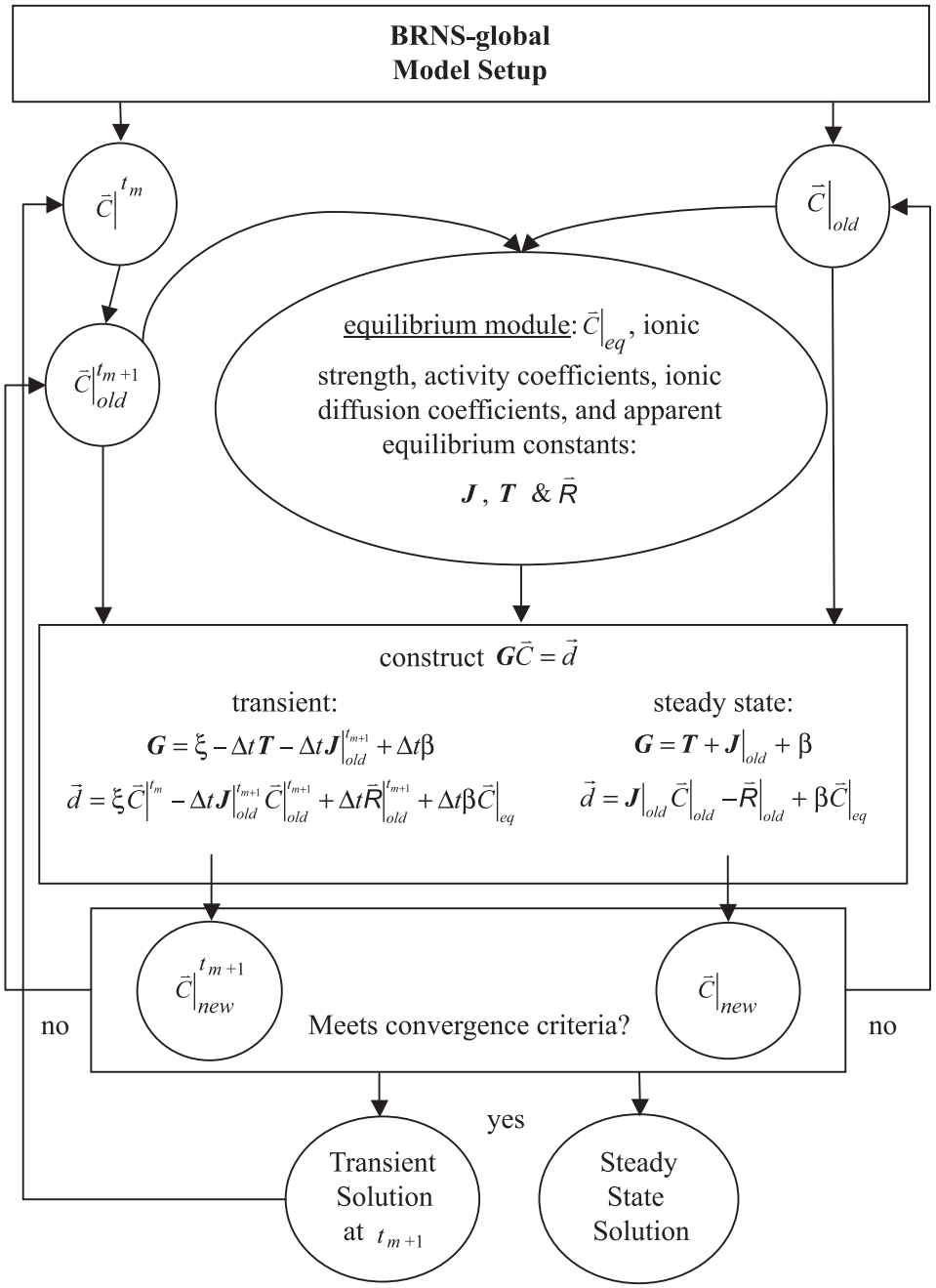

Fig. 1. Schematic flow chart of the global implicit solver.

and $\vec{d}$ is a vector of length N. The block matrices, $\boldsymbol{G}^j$ (j = 1 to N_x), are each of dimension N_s by N_s. The proposed iterative procedure for the numerical solution of transient and steady state simulations is summarized in figure 1.

The reaction network is implemented in the Biogeochemical Reaction Network Simulator (BRNS©), a flexible simulation environment for multicomponent reaction transport calculations (Regnier and others, 2002; Aguilera and others, 2005; see also www.geo.uu.nl/~kbrtm). All the reactions, transport processes, parameter values, boundary conditions and physical domain characteristics are defined by the user via a Maple© interface worksheet. An automatic code generator (ACG) then produces and compiles the corresponding FORTRAN code, providing the user with the corresponding model executable. In particular, for any reactive transport application, the ACG automatically constructs the elements of the Jacobian matrix plus enables the construction of $\boldsymbol{G}$ and $\bar{d}$. It is a modified version of the ACG presented in Aguilera and others, 2005, where further details about the methodology are provided. As the proposed approach facilitates modification and expansion of the reaction network, the BRNS is a particularly flexible tool for the reactive transport simulation of complex biogeochemical problems.

APPLICATION

The proposed modeling approach is used to compute the vertical distributions of pH and proton production/consumption rates in a model sediment representative of depositional environments encountered on the continental shelves. A major goal of the application is to illustrate how pH depth profiles can be interpreted in terms of proton production or consumption by the various biogeochemical processes in the sediment. Sediment properties, the reaction network, and reaction plus transport parameters are taken from Van Cappellen and Wang (1995). The main differences with the simulations presented by these authors are the inclusion of calcite dissolution and boric acid dissociation in the reaction network.

First, results of a baseline simulation are shown in which pore water irrigation is omitted ($\alpha = 0$, *Baseline Model Setup and Simulation Results* section). Second, the proton production and consumption rates (as described in the *Stoichiometric Coefficients* section, eq 12) are used in the interpretation of the model predicted pH profile (*Proton Production and Consumption Rates* section). The *Sulfur Cycling* section presents an analysis of the effects of sulfate reduction and sulfur cycling on pH and calcite saturation. Finally, in the *Calcite Dissolution* and *Irrigation* sections the effects of calcite dissolution and pore water irrigation on the pH distribution are further explored.

For simplicity, we limit ourselves to steady state simulations. Due to the high ionic strength and uniform electrolyte composition of seawater, which mask changes of the pore water ionic medium due to early diagenetic reactions, we further assume that the apparent acid dissociation constants do not vary with depth. This assumption may no longer be valid in nearshore settings where variations in sulfate concentration may significantly change the ionic composition, and thereby affect the total hydrogen ion concentration (Gaillard and others, 1989; see also *Sulfur Cycling* section). The contribution of protons and hydroxyl ions to total alkalinity are assumed to be negligible. The resulting pH and alkalinity profiles provide *a posteriori* validation of this assumption for all the simulation results presented.

The use of mass conservation equation (1) requires a consistent set of units for the specification of mass, length, and time. In the definition of model parameters and presentation of the simulation results, we use units of years for time, g for mass, and moles in specifying the concentration units. Whereas the length units of cm are commonly used in the specification of the physical parameters (for example, sedimentation rate, diffusion coefficient), the more convenient unit of dm^3 (that is, L) is used in specifying the solute concentrations. Furthermore, the unit of moles per gram of solid sediment (rather than per cm^3) is used to define the concentrations of the solid

species, by assuming a constant density for the solid sediment (ρ_s). As such, the mass balance equations are further scaled by $1/\rho_s$ for the solids and $\frac{1000 cm^3}{1L}$ for the solutes.

Baseline Model Setup and Simulation Results

Most chemical and biological transformations occurring in marine sediments are linked to the oxidation of deposited organic matter (Berner, 1980). The pathways of organic carbon oxidation are therefore referred to as the primary redox reactions (Van Cappellen and Gaillard, 1996). These reactions proceed in the order of decreasing free energy yield and result in the production of reduced chemical species, for example, NH_4^+, Mn^{2+}, Fe^{2+}, HS^-, and CH_4. The upward migration of the reduced species into more oxidizing sediment layers causes their re-oxidation via a set of secondary redox reactions, which sustain a continuous, early diagenetic cycle of redox-sensitive elements such as N, S, Fe and Mn. Especially for iron, manganese and sulfur, the redox cycles involve the dissolution and precipitation of mineral phases.

An important mineral dissolution/precipitation system is that of calcium carbonate. While, strictly speaking, the dissolution and precipitation reactions of $CaCO_3$ are not redox-dependent, variations in the saturation state of pore waters with respect to calcite are intimately linked to the network of primary and secondary redox reactions through their effects on T_A and T_C (Hales, 2003). In the simulations performed here, calcite dissolution is included as a possible reaction pathway, with a rate that depends on the degree of pore water undersaturation. It is assumed that the sediments are deposited in bottom waters that are moderately supersaturated with respect to calcite.

The reaction network of primary and secondary redox processes, non-redox mineral precipitation or dissolution reactions, plus the acid-base equilibria of the carbonate, sulfide, and boric acid systems, considered in the baseline scenario is summarized in table 4. It contains a total of 24 reaction pathways and 23 individual species. Although additional reaction processes and species are important, the set of reactions in table 4 captures the essence of the redox and acid-base dynamics of early diagenesis in marine sediments. The baseline sediment model thus serves to illustrate the potential use of reaction transport modeling as a diagnostic tool for interpreting pore water pH profiles. Chemical species that participate in the equilibrium reactions are represented in the reaction formulas of the kinetically-controlled processes with their variable stoichiometric coefficients, s^i_{keq}. The (fixed) stoichiometric coefficients describing production of T_C, T_S and T_A by the kinetic reactions are listed in table 5. The rate laws for the kinetic reactions and the equilibrium conditions for the homogeneous acid-base reactions are given in table 6.

At the upper boundary (SWI), fixed concentrations are assigned to the solute species, while deposition fluxes are specified for the solid species (table 7). The lower boundary conditions are defined at a sufficiently great depth, such that all concentration gradients vanish as reaction rates approach zero. The molecular diffusion coefficients listed in table 7 are adjusted for the viscosity and temperature of the bottom water (for details, see Van Cappellen and Wang, 1995; and Boudreau, 1997). Tables 8 and 9 provide all the physical and reaction model parameters, plus the domain definition. Equilibrium constants are corrected for the pressure, temperature, and salinity conditions at the seafloor (Millero and Sohn, 1992; Wang and Van Cappellen, 1996; Pilson, 1998).

The simulated depth distributions of concentrations of chemical species and components are presented in figures 2 to 4. On the basis of the model results, three chemical redox zones can be delineated; the oxic (0–1.5 cm), suboxic (1.5–3.2 cm) and anoxic (>3.2 cm) zone. The oxic/suboxic interface is defined here as the depth at

TABLE 4

The reaction network

Primary Redox Reactions
R^1. oxic respiration $(CH_2O)(NH_3)_y(H_3PO_4)_z + O_2 \rightarrow \sum_{keq} s^1_{keq} C_{keq} + yNH_4^+ + zHPO_4^{2-}$
R^2. denitrification $(CH_2O)(NH_3)_y(H_3PO_4)_z + [(4+3y)/5]NO_3^- \rightarrow \sum_{keq} s^2_{keq} C_{keq} + [(2+4y)/5]N_2 + zHPO_4^{2-}$
R^3. Mn(IV) reduction $(CH_2O)(NH_3)_y(H_3PO_4)_z + 2MnO_2 \rightarrow \sum_{keq} s^3_{keq} C_{keq} + 2Mn^{2+} + yNH_4^+ + zHPO_4^{2-}$
R^4. Fe(III) reduction $(CH_2O)(NH_3)_y(H_3PO_4)_z + 4Fe(OH)_3 \rightarrow \sum_{keq} s^4_{keq} C_{keq} + 4Fe^{2+} + yNH_4^+ + zHPO_4^{2-}$
R^5. sulfate reduction $(CH_2O)(NH_3)_y(H_3PO_4)_z + (1/2)SO_4^{2-} \rightarrow \sum_{keq} s^5_{keq} C_{keq} + yNH_4^+ + zHPO_4^{2-}$
R^6. methanogenesis $(CH_2O)(NH_3)_y(H_3PO_4)_z \rightarrow \sum_{keq} s^6_{keq} C_{keq} + yNH_4^+ + zHPO_4^{2-} + (1/2)CH_4$
Secondary Redox Reactions
R^7. nitrification $NH_4^+ + 2O_2 \rightarrow \sum_{keq} s^7_{keq} C_{keq} + NO_3^-$
R^8. Mn^{2+} re-oxidation by O_2 $Mn^{2+} + (1/2)O_2 \rightarrow \sum_{keq} s^8_{keq} C_{keq} + MnO_2$
R^9. Fe^{2+} re-oxidation by O_2 $Fe^{2+} + (1/4)O_2 \rightarrow \sum_{keq} s^9_{keq} C_{keq} + Fe(OH)_3$
R^{10}. Fe^{2+} re-oxidation by MnO_2 $2Fe^{2+} + MnO_2 \rightarrow \sum_{keq} s^{10}_{keq} C_{keq} + 2Fe(OH)_3 + Mn^{2+}$
R^{11}. sulfide re-oxidation by O_2 $2O_2 \rightarrow \sum_{keq} s^{11}_{keq} C_{keq} + SO_4^{2-}$
R^{12}. sulfide re-oxidation by MnO_2 $MnO_2 \rightarrow \sum_{keq} s^{12}_{keq} C_{keq} + Mn^{2+} + S^0$
R^{13}. sulfide re-oxidation by $Fe(OH)_3$ $2Fe(OH)_3 \rightarrow \sum_{keq} s^{13}_{keq} C_{keq} + 2Fe^{2+} + S^0$
R^{14}. methane re-oxidation by O_2 $CH_4 + 2O_2 \rightarrow \sum_{keq} s^{14}_{keq} C_{keq}$
R^{15}. methane re-oxidation by SO_4^{2-} $CH_4 + SO_4^{2-} \rightarrow \sum_{keq} s^{15}_{keq} C_{keq}$
R^{16}. FeS re-oxidation by O_2 $FeS + 2O_2 \rightarrow Fe^{2+} + SO_4^{2-}$

TABLE 4
(continued)

Mineral Precipitation / Dissolution
R^{17}. $CaCO_3$ dissolution $CaCO_3 \rightarrow \sum_{keq} s^{17}_{keq} C_{keq} + Ca^{2+}$
R^{18}. FeS precipitation $Fe^{2+} \rightarrow \sum_{keq} s^{18}_{keq} C_{keq} + FeS$
R^{19}. $MnCO_3$ precipitation $Mn^{2+} \rightarrow \sum_{keq} s^{19}_{keq} C_{keq} + MnCO_3$
R^{20}. $FeCO_3$ precipitation $Fe^{2+} \rightarrow \sum_{keq} s^{20}_{keq} C_{keq} + FeCO_3$
Equilibrium Conditions
Eq1. carbonic acid dissociation $H_2O + CO_2 \leftrightarrow HCO_3^- + H^+$
Eq2. bicarbonate dissociation $HCO_3^- \leftrightarrow CO_3^{2-} + H^+$
Eq3. sulfide dissociation $H_2S \leftrightarrow HS^- + H^+$
Eq4. boric acid dissociation $B(OH)_3 + H_2O \leftrightarrow B(OH)_4^- + H+$

For each kinetic reaction, i, the sum of species involved in the equilibrium conditions are expressed as:

$$\sum_{keq} s^i_{keq} C_{keq} = s^i_{co2}[CO_2] + s^i_{hco3}[HCO_3^-] + s^i_{co3}[CO_3^{2-}] + s^i_{h2s}[H_2S] + s^i_{hs}[HS^-] + s^i_{boh3}[B(OH)_3] + s^i_{boh4}[B(OH)_4^-] + s^i_h[H^+] + s^i_{oh}[OH^-]$$

where the stoichiometric coefficients of total components:

$$t^i_c = s^i_{co2} + s^i_{hco3} + s^i_{co3}$$

$$t^i_a = s^i_{hco3} + 2s^i_{co3} + s^i_{hs} + s^i_{boh4} + s^i_{oh} - s^i_h$$

$$t^i_s = s^i_{h2s} + s^i_{hs}$$

are given in table 5; y and z denote the nitrogen to carbon ratio (N:C) and the phosphorus to carbon ratio (P:C) of the degrading organic matter, respectively.

which the aerobic respiration and denitrification rates are equal (not shown). Similarly, the suboxic/anoxic interface is defined as the depth at which the dissimilarity Fe(III) reduction and sulfate reduction rates are equal (not shown). Figure 4 shows that the depth profiles of pH and the concentrations of dissolved carbonate and borate species exhibit marked changes at these interfaces, hence illustrating the close coupling of redox and acid-base chemistry in the reaction transport system. The apparent activity coefficient of protons (f_{H+} in table 9) is used to display pH on the NBS scale.

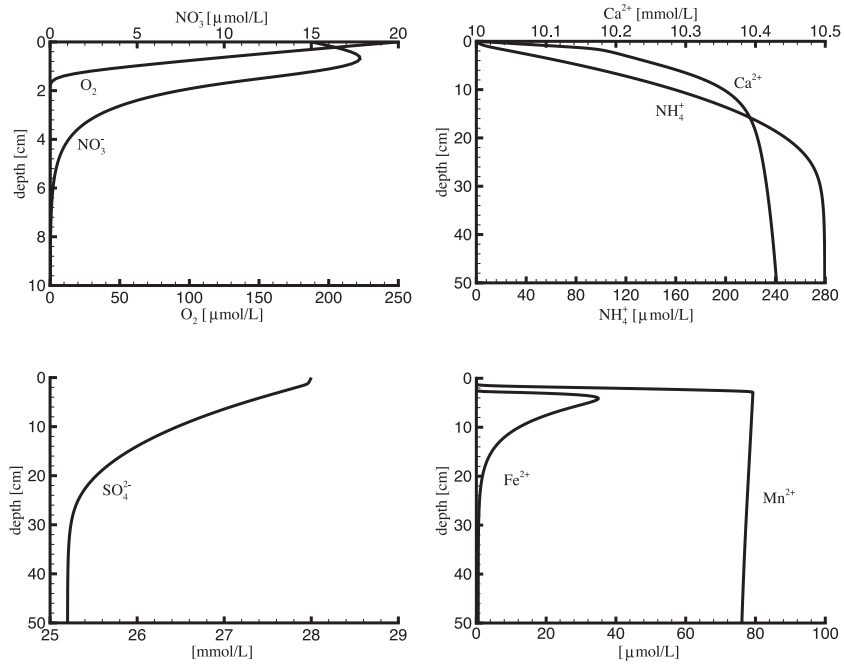

Fig. 2. Distributions of the non-protolytic solute species in the baseline simulation. Sulfate approaches a finite constant value at depth, when all of the reactive organic matter is degraded (fig. 3). Aqueous Fe and Mn concentrations build up in the suboxic layer and decrease in the anoxic zone by mineral precipitation reactions (see text).

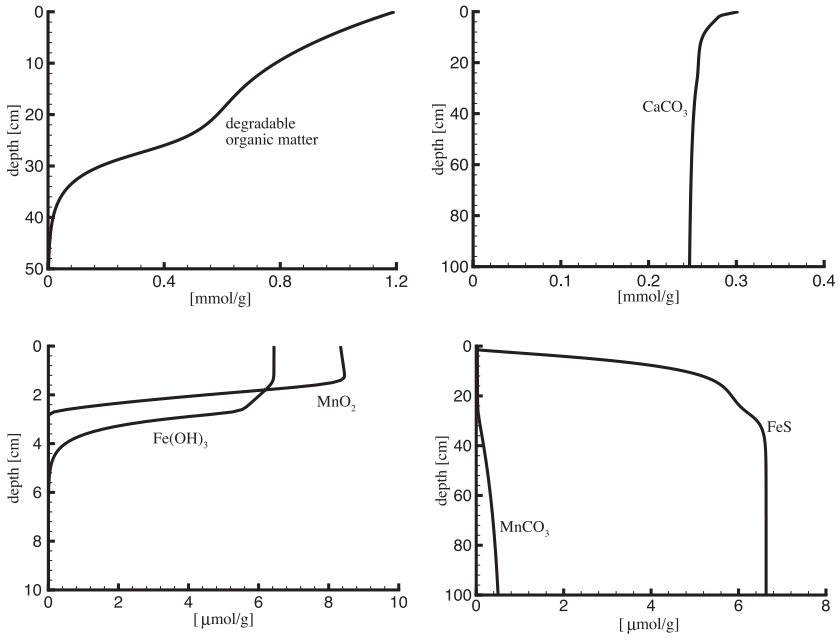

Fig. 3. Distributions of the solid species in the baseline simulation. Nearly all reactive organic carbon is degraded in the top 50 cm of the sediment, while 75% of calcite reaching the sediment dissolves in the top 15 cm. Precipitation of carbonate and sulfide minerals act as permanent sinks of reactive Fe and Mn (see text).

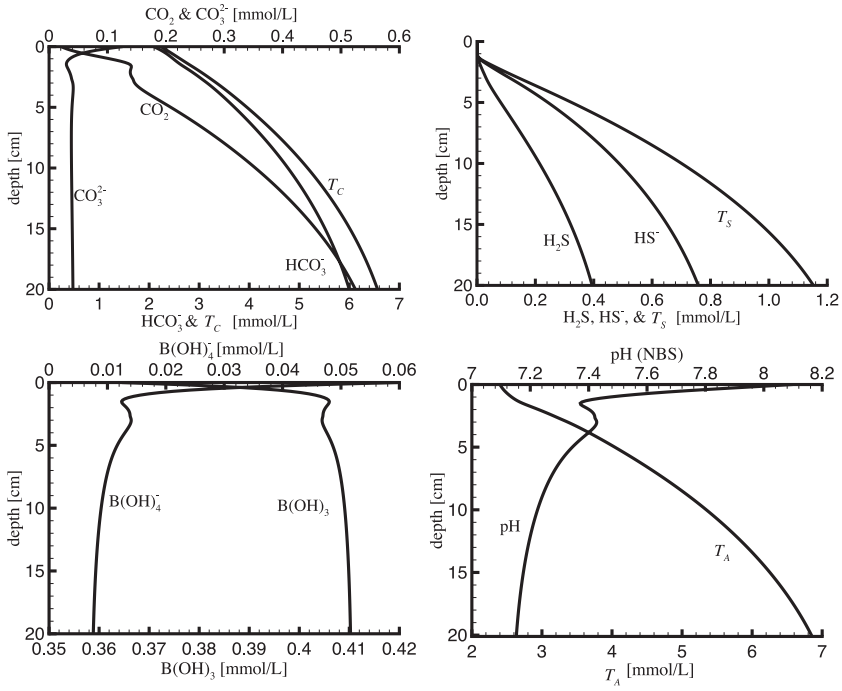

Fig. 4. Pore water distributions of protolytic species, total dissolved inorganic carbon (T_C), total alkalinity (T_A), total sulfides (T_S), and pH in the baseline scenario. The pH profile exhibits a local minimum at the oxic/suboxic interface (1.5 cm) and a local maximum at 3.0 cm near the suboxic/anoxic interface (3.2 cm).

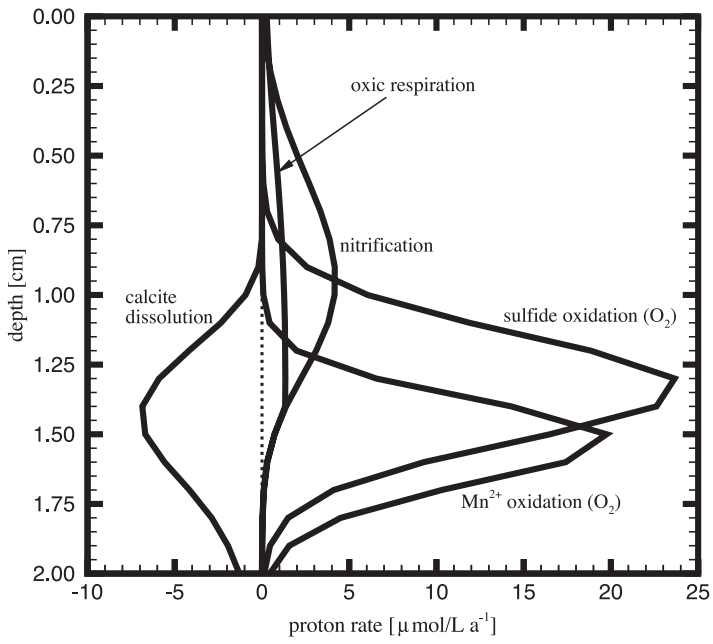

Fig. 5. Proton rates in the oxic zone: results of the baseline simulation.

Table 5

Stoichiometric coefficients of the components for each reaction i: the components refer to total dissolved inorganic carbon (t_c^i) total alkalinity (t_a^i), and total sulfides (t_s^i)

Reaction i	t_c^i	t_a^i	t_s^i
R^1	1	(y-2z)	0
R^2	1	(4+3y-10z)/5	0
R^3	1	(4+y-2z)	0
R^4	1	(8+y-2z)	0
R^5	1	(1+y-2z)	1/2
R^6	1/2	(y-2z)	0
R^7	0	-2	0
R^8	0	-2	0
R^9	0	-2	0
R^{10}	0	-2	0
R^{11}	0	-2	-1
R^{12}	0	2	-1
R^{13}	0	4	-1
R^{14}	1	0	0
R^{15}	1	2	1
R^{16}	0	0	0
R^{17}	1	2	0
R^{18}	0	-2	-1
R^{19}	-1	-2	0
R^{20}	-1	-2	0

While a direct comparison of model predicted pH profiles with measured profiles is beyond the scope of this paper, it is worth noting that the major features of the pH profile of our baseline simulation are consistent with published pore water pH data sets. In particular, the reader is referred to the studies of Cai and Reimers (1993), Cai and others (1995, 2000), Hensen and others (1997), Luff and others (2000), Adler and others (2001), Wenzhöfer and others (2001), Wijsman and others (2002), and Forja and others (2004). These studies show that a sharp drop in pH near the SWI followed by a local minimum in pH deeper in the sediment is commonly seen in marine sediments overlain by oxygenated waters, from coastal to deep-sea environments.

All the degradable organic carbon in the baseline scenario is oxidized in the top 50 cm of the sediment (fig. 3) at which point a high dissolved sulfate concentration remains (fig. 2). Thus, in this particular early diagenetic scenario, methanogenesis is inhibited and no methane is produced. Oxic degradation and secondary redox reactions with NH_4^+, Fe^{2+} and Mn^{2+} deplete oxygen in the first few centimeters of the sediment (fig. 2). The interplay between denitrification and nitrification reactions results in the occurrence of a peak in the nitrate profile near the sediment water interface, while NH_4^+ released from the degradation of organic carbon builds up with depth into the sediment (fig. 2). Calcite dissolution increases the pore water calcium ion concentrations by about 4 percent relative to the overlying seawater (fig. 2).

A significant fraction of the deposited calcite dissolves, most of it in the upper 15 cm (fig. 3). That is, pore water pH buffering by $CaCO_3$ dissolution extends well below the oxic zone of the sediment. In the anoxic zone, iron sulfide precipitation causes the near complete removal of dissolved Fe^{2+} from the pore waters (figs. 2 and 3). In contrast, dissolved Mn^{2+} builds up to high levels, because of less efficient removal by $MnCO_3$ precipitation. As a result, most dissolved Mn^{2+} returns to the oxic zone where it oxidatively precipitates. This explains why the concentrations of reactive Mn oxide

exceed those of reactive Fe oxide (fig. 3), despite the lower deposition flux of reactive Mn oxide (table 7).

Proton Production and Consumption Rates

In what follows, the model-predicted pH profile (fig. 4) is interpreted in terms of the rates of production and consumption of H^+ by the various biogeochemical reactions taking place in the sediment (eq 12). Figures 5 and 6 present the depth profiles of the dominant proton rates in the oxic and suboxic plus anoxic zones, respectively. Note that variable depth and rate scales are used in order to highlight the important features of the profiles.

As systematically found in marine sediments deposited under oxygenated bottom waters, the model-derived pH profile exhibits a sharp decrease just below the SWI (see, for example, Cai and others, 1995; Hales and others, 1997a; Cai and others, 2000; Wenzhöfer and others, 2001; Wijsman and others, 2002; Forja and others, 2004). This pH drop is usually attributed to carbonic acid production by oxic respiration. However, in the model sediment considered, secondary oxygenation reactions play an even greater role than aerobic respiration of organic matter in generating H^+ (fig. 5). This is particularly true at the bottom of the oxic zone, where sulfide and Mn^{2+} oxidation by O_2 are the main sources of H^+. At these depths ($\sim$1 cm), the pore waters become undersaturated with respect to calcite, and $CaCO_3$ dissolution partly buffers the drop in pH (see *Calcite Dissolution* section). Overall, net production of H^+ in the oxic zone causes the pH to reach a local minimum near the depth where pore water O_2 disappears.

In the suboxic zone, intense calcite dissolution in the 1 to 2 cm depth interval offsets H^+ production by denitrification and Fe^{2+} oxidation in the same depth interval (fig. 6). Sulfide oxidation coupled to reduction of Fe and Mn oxides, and dissimilatory Fe(III) and Mn(IV) reduction further consume protons within the suboxic zone, while Fe^{2+} oxidation coupled to Mn oxide reduction is the principal proton producing process in this zone. Precipitation of authigenic $MnCO_3$ is a minor source of H^+.

The suboxic zone is characterized by a pH minimum (fig. 4). The appearance of a reversal in the pH versus depth trend in the suboxic zone can be attributed to the reductive dissolution of iron and manganese (hydr)oxides coupled to organic matter and sulfide oxidation. This is shown in figure 7, where the pH distribution of the baseline scenario is compared to that of a simulation with no input of Fe and Mn (hydr)oxides at the sediment-water interface. In the latter case, no reversal of the pH trend below the oxic zone is observed. As also proposed by Van Cappellen and Wang (1996), the presence of a pronounced pH minimum below the oxic zone is a diagnostic feature of intense redox cycling of Fe and Mn.

Within the anoxic zone, the pH decreases with depth as a result of sulfate reduction and, to a lesser extent, iron sulfide precipitation (fig. 6). As a consequence, the pH profile shows a characteristic subsurface maximum in the suboxic zone. The pH continues to decrease until a depth of around 50 cm (not shown), where all degradable organic matter is consumed. In the anoxic zone, the pore waters remain undersaturated with respect to $FeCO_3$, near saturation with respect to $MnCO_3$, and slightly undersaturated with respect to calcite (fig. 8). Slow dissolution of calcite at depths $>$ 50 cm causes a slight rise in pH with depth (not shown).

By combining the proton rates of the various biogeochemical processes, the net rate of proton production/consumption can be calculated as a function of depth below the SWI. In figure 9, the resulting net rate profile is broken down in a number of depth intervals. Note that the solid lines correspond to the baseline scenario. Comparison of the rate scales for the different depth intervals clearly shows that the most intense H^+ production and consumption is concentrated in the uppermost 5 centimeters of the sediment. In this depth interval, the net rate profile shows a close succession

TABLE 6

Kinetic reaction rate laws and equilibrium massaction laws for the baseline simulation

Kinetic Rate Laws
$R^1 = f_{O_2} k_c [CH_2O](1-\phi)\rho_s$, where $\begin{cases} f_{O_2} = 1 \text{ for } [O_2] > K_{O2} \\ f_{O_2} = \dfrac{[O_2]}{K_{O2}} \text{ for } [O_2] \le K_{O2} \end{cases}$
$R^2 = f_{NO_3^-} k_c [CH_2O](1-\phi)\rho_s$, where $\begin{cases} f_{NO_3^-} = 0 \text{ for } f_{O_2} = 1 \\ f_{NO_3^-} = (1 - f_{O_2}) \text{ for } f_{O_2} < 1 \text{ and } [NO_3^-] > K_{NO3} \\ f_{NO_3^-} = (1 - f_{O_2}) \dfrac{[NO_3^-]}{K_{NO3}} \text{ for } f_{O_2} < 1 \text{ and } [NO_3^-] \le K_{NO3} \end{cases}$
$R^3 = f_{MnO_2} k_c [CH_2O](1-\phi)\rho_s$, where $\begin{cases} f_{MnO_2} = 0 \text{ for } f_3 \equiv f_{O_2} + f_{NO_3^-} = 1 \\ f_{MnO_2} = (1 - f_3) \text{ for } f_3 < 1 \text{ and } [MnO_2] > K_{MnO2} \\ f_{MnO_2} = (1 - f_3) \dfrac{[MnO_2]}{K_{MnO2}} \text{ for } f_3 < 1 \text{ and } [MnO_2] \le K_{MnO2} \end{cases}$
$R^4 = f_{Fe(OH)_3} k_c [CH_2O](1-\phi)\rho_s$, where $\begin{cases} f_{Fe(OH)_3} = 0 \text{ for } f_4 \equiv f_{O_2} + f_{NO_3^-} + f_{MnO_2} = 1 \\ f_{Fe(OH)_3} = (1 - f_4) \text{ for } f_4 < 1 \text{ and } [Fe(OH)_3] > K_{FeOH3} \\ f_{Fe(OH)_3} = (1 - f_4) \dfrac{[Fe(OH)_3]}{K_{FeOH3}} \text{ for } f_4 < 1 \text{ and } [Fe(OH)_3] \le K_{FeOH3} \end{cases}$
$R^5 = f_{SO_4^{2-}} k_c [CH_2O](1-\phi)\rho_s$, where $\begin{cases} f_{SO_4^{2-}} = 0 \text{ for } f_5 \equiv f_{O_2} + f_{NO_3^-} + f_{MnO_2} + f_{Fe(OH)_3} = 1 \\ f_{SO_4^{2-}} = (1 - f_5) \text{ for } f_5 < 1 \text{ and } [SO_4^{2-}] > K_{SO4} \\ f_{SO_4^{2-}} = (1 - f_5) \dfrac{[SO_4^{2-}]}{K_{SO4}} \text{ for } f_5 < 1 \text{ and } [SO_4^{2-}] \le K_{SO4} \end{cases}$
$R^6 = \left(1 - f_{O_2} - f_{NO_3^-} - f_{MnO_2} - f_{Fe(OH)_3} - f_{SO_4^{2-}}\right) k_c [CH_2O](1-\phi)\rho_s$
$R^7 = k_7 [NH_4^+][O_2]\phi\left(\dfrac{1L}{10^3 cm^3}\right)$
$R^8 = k_8 [Mn^{2+}][O_2]\phi\left(\dfrac{1L}{10^3 cm^3}\right)$
$R^9 = k_9 [Fe^{2+}][O_2]\phi\left(\dfrac{1L}{10^3 cm^3}\right)$
$R^{10} = k_{10} [Fe^{2+}][MnO_2](1-\phi)\rho_s$
$R^{11} = k_{11} [O_2]\left([H_2S] + [HS^-]\right)\phi\left(\dfrac{1L}{10^3 cm^3}\right)$
$R^{12} = k_{12} [MnO_2]\left([H_2S] + [HS^-]\right)(1-\phi)\rho_s$
$R^{13} = k_{13} [Fe(OH)_3]\left([H_2S] + [HS^-]\right)(1-\phi)\rho_s$

TABLE 6

(continued)

$$R^{14} = k_{14}[CH_4][O_2]\phi\left(\frac{1L}{10^3 cm^3}\right)$$

$$R^{15} = k_{15}[CH_4][SO_4^{2-}]\phi\left(\frac{1L}{10^3 cm^3}\right)$$

$$R^{16} = k_{16}[FeS][O_2](1-\phi)\rho_s$$

$$R^{17} = \begin{cases} 0 \text{ for } \Omega_{17} \equiv \dfrac{[Ca^{2+}][CO_3^{2-}]}{K_{s17}} > 1 \\ k_{17}[CaCO_3](1-\Omega_{17})^{\prime}(1-\phi)\rho_s \text{ for } \Omega_{17} \le 1 \end{cases}$$

$$R^{18} = \begin{cases} 0 \text{ for } \Omega_{18} \equiv \dfrac{[Fe^{2+}][HS^-]}{[H^+]K_{s18}} \le 1 \\ k_{18}(\Omega_{18}-1)\,\phi\left(\dfrac{1L}{10^3 cm^3}\right) \text{ for } \Omega_{18} > 1 \end{cases}$$

$$R^{19} = \begin{cases} 0 \text{ for } \Omega_{19} \equiv \dfrac{[Mn^{2+}][CO_3^{2-}]}{K_{s19}} \le 1 \\ k_{19}(\Omega_{19}-1)\,\phi\left(\dfrac{1L}{10^3 cm^3}\right) \text{ for } \Omega_{19} > 1 \end{cases}$$

$$R^{20} = \begin{cases} 0 \text{ for } \Omega_{20} \equiv \dfrac{[Fe^{2+}][CO_3^{2-}]}{K_{s20}} \le 1 \\ k_{20}(\Omega_{20}-1)\,\phi\left(\dfrac{1L}{10^3 cm^3}\right) \text{ for } \Omega_{20} > 1 \end{cases}$$

Mass Action Laws

$$Eq1: K_1^* = \frac{[H^+][HCO_3^-]}{[CO_2]}$$

$$Eq2: K_2^* = \frac{[H^+][CO_3^{2-}]}{[HCO_3^-]}$$

$$Eq3: K_4^* = \frac{[H^+][HS^-]}{[H_2S]}$$

$$Eq4: K_5^* = \frac{[H^+][B(OH)_4^-]}{[B(OH)_3]}$$

Formulations taken from Van Cappellen and Wang (1995) with the exception of R^{17} for calcite dissolution, which is adapted from Keir (1980). All parameter values are specified in table 9. The species concentrations are defined in units of moles per gram of solid sediment and moles per liter of pore water volume for the solids and solutes, respectively. For simplicity, the concentration of $(CH_2O)(NH_3)_y(H_3PO_4)_z$ is denoted by $[CH_2O]$.

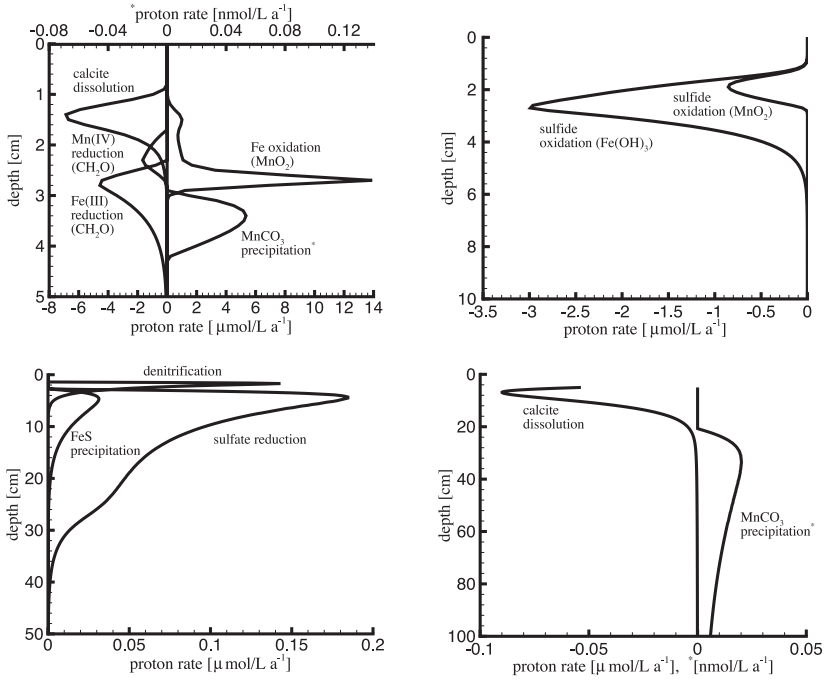

Fig. 6. Proton rates in the suboxic and anoxic zones: results of the baseline simulation. Note that variable scales are used for the depth and rates in order to highlight the main features of the profiles.

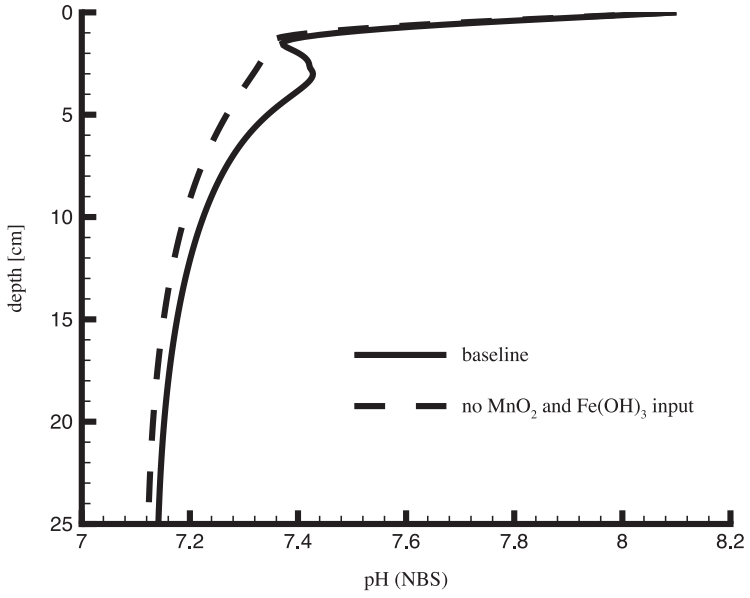

Fig. 7. pH profiles in the baseline simulation (solid line) and in the absence of deposition of reactive Fe and Mn (hydr)oxides (broken line).

TABLE 7

Species, boundary conditions, and molecular diffusion coefficients used in the baseline simulation

Species	Upper Boundary Condition	Molecular Diffusion [$cm^2\ a^{-1}$]
O_2	250	459
NO_3^-	15	411
HCO_3^-	2088	243
CO_3^{2-}	126	195
CO_2	21	386
H^+	$(10^{-8.1})/f_{H+}$	-
CH_2O	80 (F)	0
Ca^{2+}	10^4	165
$CaCO_3$	20 (F)	0
NH^{4+}	0	421
SO_4^{2-}	28×10^3	190
Mn^{2+}	0	140
MnO_2	1.2×10^{-2} (F)	0
Fe^{2+}	0	148
$Fe(OH)_3$	10^{-1} (F)	0
H_2S	0	400
HS^-	0	388
FeS	0 (F)	0
$FeCO_3$	0 (F)	0
$MnCO_3$	0 (F)	0
CH_4	0	303
$B(OH)_3$	60	123
$B(OH)_4^-$	365	108

The boundary condition is specified as fixed concentration in units of μmoles L^{-1} porewater for solute species, and as flux (F) for all solid species in units of μmoles $cm^{-2}\ a^{-1}$. The boundary conditions are taken from Van Cappellen and Wang (1995) except for the flux of calcite and the concentration of total borates; Flux of calcite is taken from Tsunogoi and Noriki (1991) for a water depth of 130 m; Total borates is calculated as a function of salinity according to Millero and Sohn (1992). See table 9 for the activity coefficient of protons, f_{H^+}. The molecular diffusion coefficients are adapted from Li and Gregory (1974), Lerman (1979), Boudreau and Canfield (1993), and Iverson and Jørgensen (1993). The temperature, salinity, porosity, and pressure corrections were carried out according to Boudreau (1997).

TABLE 8

Physical parameters used in the baseline simulation

Burial (ω)	0.04	$cm\ a^{-1}$
Bioturbation coefficient at SWI (D_{b0})	3	$cm^2\ a^{-1}$
Porosity (ϕ)	0.85	
Temperature (T)	10	°C
Pressure (P)	13	bar
Salinity (S)	35	‰
Number of nodes (N_x)	251	
Max depth	165	cm
Solid density (ρ_s)	2.5	$g\ cm^{-3}$
Fluid density (ρ_f)	1027.5	$kg\ m^{-3}$
α_k	0	$cm\ a^{-1}$

The bioturbation coefficient, D_b is a function of depth, x in cm: $D_b(x) = \frac{D_{b0}}{2}\,\mathrm{erfc}\left(\frac{(x-20)}{4}\right)$, where erfc is the complementary error function. A variable grid spacing that ranges from 0.1 cm at SWI to 2.0 cm at depth is used here. Burial rate, porosity, temperature, and solid density are taken from Van Cappellen and Wang (1995). The pressure is calculated from UNESCO web site, assuming a seafloor depth of 130 m as representative of shelf sediments (Millero and Sohn, 1992). Fluid density for the given temperature, pressure, and salinity taken from UNESCO equation of state (Chester, 2000).

Table 9

Parameters for the reaction network and stoichiometric coefficients

Parameter Name	Parameter Value	Units	Reaction(s)
k_c	10^{-2}	a^{-1}	1-6
K_{O2}	8×10^{-6}	mol/L	1-6
K_{NO3}	10^{-5}	mol/ L	2-6
K_{MnO2}	2×10^{-6}	mol/g	3-6
K_{FeOH3}	5×10^{-6}	mol/g	4-6
K_{SO4}	10^{-3}	mol/L	5-6
y (N:C)	21/200		1-6
z (P:C)	1/200		1-6
k_7	1.5×10^{7}	L mol^{-1} a^{-1}	7
k_8	2×10^{9}	L mol^{-1} a^{-1}	8
k_9	2×10^{9}	L mol^{-1} a^{-1}	9
k_{10}	2×10^{8}	L mol^{-1} a^{-1}	10
k_{11}	6×10^{8}	L mol^{-1} a^{-1}	11
k_{12}	10^{4}	L mol^{-1} a^{-1}	12
k_{13}	10^{4}	L mol^{-1} a^{-1}	13
k_{14}	10^{10}	L mol^{-1} a^{-1}	14
k_{15}	10^{10}	L mol^{-1} a^{-1}	15
k_{16}	2.2×10^{7}	L mol^{-1} a^{-1}	16
K_{s17}	4.42×10^{-7}	mol^2 kg^{-2}	17
k_{17}	18.3	a^{-1}	17
n	4.5		17
k_{18}	5×10^{-6}	mol L^{-1} a^{-1}	18
k_{19}	10^{-5}	mol L^{-1} a^{-1}	19
k_{20}	10^{-6}	mol L^{-1} a^{-1}	20
K_{s18}	$(6.3 \times 10^{-3})\, f_{H+}$	mol/L	18
K_{s19}	3.2×10^{-9}	mol^2 L^{-2}	19
K_{s20}	4×10^{-9}	mol^2 L^{-2}	20
f_{H+}	0.77		
K_1^*	$(8.05 \times 10^{-7})/f_{H+}$	mol/L	Eq1
K_2^*	$(4.8 \times 10^{-10})/f_{H+}$	mol/L	Eq2
K_4^*	$(1.35 \times 10^{-7})/f_{H+}$	mol/L	Eq4
K_5^*	$(1.3 \times 10^{-9})/f_{H+}$	mol/L	Eq5

See text for rate constant of calcite dissolution and rate order, n. The apparent equilibrium constants (K_1^*, K_2^*, K_4^*, and K_5^*) are calculated for the given temperature, salinity and pressure based on the total hydrogen ion (seawater) scale (Stumm and Morgan, 1996; Pilson, 1998). The apparent activity coefficient of hydrated proton or hydrogen ion, f_{H^+}, is calculated for the given salinity and temperature according to Pilson, 1998.

of zones of net production and consumption of H^+. At greater depths, net proton rates are orders of magnitude slower.

The overall contribution of any given biogeochemical process to the production or consumption of protons can be ranked by integrating the corresponding proton rate with depth (table 10). The dominant proton producing process in the sediment is sulfide oxidation by O_2, in line with the observations of Boudreau (1991) and Luff and Wallmann (2003). The results further imply that proton production mainly results from secondary redox reactions. The primary redox reactions sulfate reduction and aerobic respiration are only the 5th and 6th most important processes in terms of integrated proton production. The major biogeo-

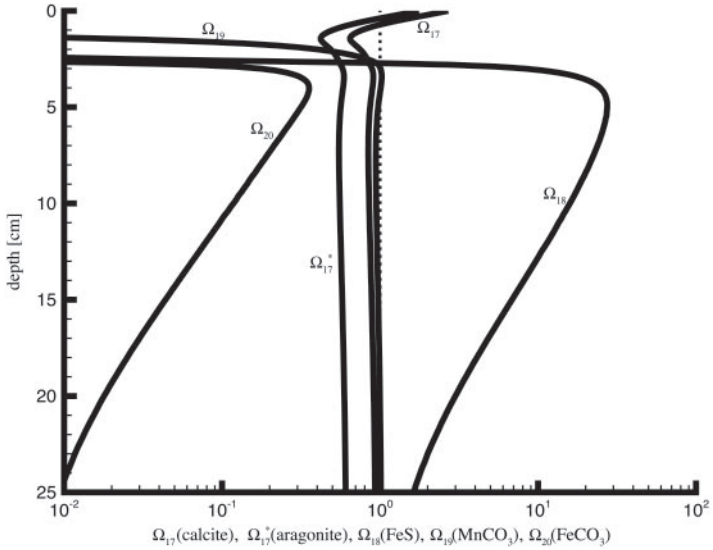

Fig. 8. Pore water saturation states with respect to $CaCO_3$, FeS, $MnCO_3$, and $FeCO_3$: results of the baseline simulation.

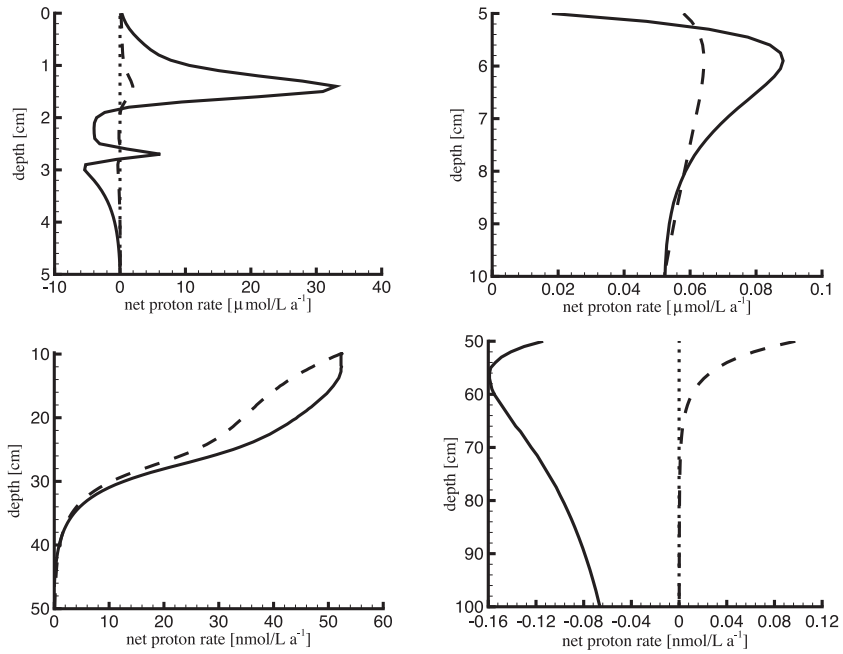

Fig. 9. Net rate of proton production (positive) and consumption (negative) in the baseline simulation (solid lines) and in a simulation assuming equilibrium with calcite (broken line). A thin dotted line indicates zero net rate. See text for complete discussion.

Table 10

Integrated proton production (positive) and consumption (negative) rates for reaction processes in the baseline simulation, in order of decreasing magnitude

Kinetic Rate Description	Integrated Rate [nmol cm^{-2} a^{-1}]
1. Sulfide oxidation by O_2 (R^{11})	10.31
2. Mn^{2+} oxidation by O_2 (R^{8})	6.84
3. Calcite dissolution (R^{17})	-4.34
4. Sulfide oxidation by $Fe(OH)_3$ (R^{13})	-4.19
5. Fe^{2+} oxidation by MnO_2 (R^{10})	3.90
6. $Fe(OH)_3$ reduction (R^{4})	-3.44
7. Nitrification (R^{7})	3.03
8. Sulfate reduction (R^{5})	1.70
9. Oxic respiration (R^{1})	1.29
10. MnO_2 reduction (R^{3})	-0.90
11. Sulfide oxidation by MnO_2 (R^{12})	-0.74
12. FeS precipitation (R^{18})	0.20
13. Denitrification (R^{2})	0.13
14. Fe^{2+} oxidation by O_2 (R^{9})	0.01
15. $MnCO_3$ precipitation (R^{19})	0.001
16. Methanogenesis (R^{6})	0.00
17. CH_4 oxidation by O_2 (R^{14})	0.00
18. CH_4 oxidation by SO_4^{2-} (R^{15})	0.00
19. FeS oxidation by O_2 (R^{16})	0.00
20. $FeCO_3$ precipitation (R^{20})	0.00

chemical reactions responsible for proton consumption are calcite dissolution and the reduction of ferric (hydr)oxides by sulfide, followed by dissimilatory Fe(III) and Mn(IV) reduction.

Sulfur Cycling

The effect of some reaction pathways on pH during early diagenesis is straightforward. For example, aerobic respiration decreases pore water pH and calcite dissolution increases pore water pH. Other processes of particular importance in marine sediments, such as sulfate reduction, may have a more complex influence on pH. Depending on the local pH, the production of alkalinity by sulfate reduction, coupled to the increase in total dissolved sulfide (T_S), can result in either a production or consumption of protons (Ben-Yaakov, 1973; Mackenzie and others, 1995).

In the baseline simulation, sulfate reduction produces protons (fig. 6). At the pH conditions of the pore waters, the increase in T_S is accompanied by dissociation of H_2S and, hence, the release of protons (fig. 4). As Ben-Yaakov (1973) showed theoretically, the pH can increase if all sulfide produced is removed from solution, either by transport or mineral precipitation. In fact, in a closed system with no other reactions occurring concurrently, the reduced aqueous sulfur system would rapidly buffer the pore waters to a pH close to 6.9 (Wollast and Vanderborght, 1994; Mackenzie and others, 1995).

It has been argued that the production of carbonate alkalinity by sulfate reduction may increase the saturation state with respect to calcite and lead to $CaCO_3$ precipitation, despite concomitant proton production (Middelburg and others, 1990; Wollast and Vanderborght, 1994; Mucci and others, 2000; Forja and others, 2004). The

opposing effects of alkalinity and proton production on calcite saturation can be described mathematically by computing the instantaneous rate of CO_3^{2-} production. Using equations (8), (9) and (16), the latter is expressed as

$$\left.\frac{d[CO_3^{2-}]}{dt}\right|_i = t_i^i \chi_2 R^i + T_C \frac{\partial \chi_2}{\partial [H^+]} \left.\frac{d[H^+]}{dt}\right|_i, \tag{24}$$

for any given kinetically-controlled reaction *i*. The second term on the RHS of equation (24) accounts for the dependence of CO_3^{2-} ion production on the local pH value and the rate of proton production by reaction *i*.

For sulfate reduction, the first term on the RHS of equation (24) is always positive and, therefore, favors $CaCO_3$ precipitation by increasing the degree of saturation of the pore waters. Because $\frac{\partial \chi_2}{\partial [H^+]} < 0$, the second term on the RHS of equation (24) translates the production of protons by sulfate reduction into a consumption of CO_3^{2-} ions. The overall effect of sulfate reduction on $CaCO_3$ saturation thus depends on the relative magnitudes of the two terms on the RHS of equation (24).

As shown in figure 10, for the baseline simulation, the rate of CO_3^{2-} production by sulfate reduction is negative throughout the model domain. This means that the second term on the RHS of equation (24) has a larger absolute value than the first term at all depths. Thus, as far as calcite saturation is concerned, proton production by sulfate reduction outweighs alkalinity production. While these results are specific to the particular environmental setting considered, they indicate that sulfate reduction may not necessarily create conditions favorable to $CaCO_3$ precipitation.

In the baseline simulation, the decrease in sulfate concentration with depth is fairly small (11%) and can thus be assumed to have a negligible effect on the apparent equilibrium constants and the calculated proton rates. However, in organic rich environments, such as coastal sediments, the complete depletion of sulfate from the pore waters with depth represents a major change in the relative ionic composition of the aqueous medium, which may significantly affect the proton balance and calculated saturation states of the minerals (Gaillard and others, 1989). The full treatment of such systems then requires taking into account the contribution of the changes in the apparent equilibrium constants on the proton rates of the various reaction processes (eq 11 and Appendix I).

The oxidation of sulfide may also significantly affect the saturation state of pore waters with respect to $CaCO_3$ (see figs. 5 and 6). For example, at a 790 m water depth site on Hydrate Ridge, sulfide oxidation by oxygen appears to be the main driving force for shallow subsurface carbonate dissolution (Luff and Wallmann, 2003). In contrast, high pore water pH in sediments from the Baltic Sea has been attributed to sulfide oxidation coupled to reduction of Mn and Fe oxides (Carman and Rahm, 1997). As shown in this paper, the explicit computation of the rates of proton (eq 12) and carbonate ion (eq 24) production allows for a rigorous analysis of the relative contributions of various reaction pathways to the variations in pH and $CaCO_3$ saturation state of sediment pore waters.

A great advantage of the Biogeochemical Reaction Network Simulator (BRNS) is that it allows the user to easily add or remove reaction pathways. This is illustrated here by expanding the sulfur reaction network of the baseline simulation, by addition of pyritization, oxidation of pyrite by oxygen, and sulfur disproportionation. The reactions and their corresponding kinetic rate formulations, which are adopted from Berg and others, 2003, are given in table 11. Note that pyrite, FeS_2, is added as a new species, and the concentration of elemental sulfur, S^0, is now explicitly computed. Pyritization and sulfur disproportionation represent sinks for S^0, which in the original baseline

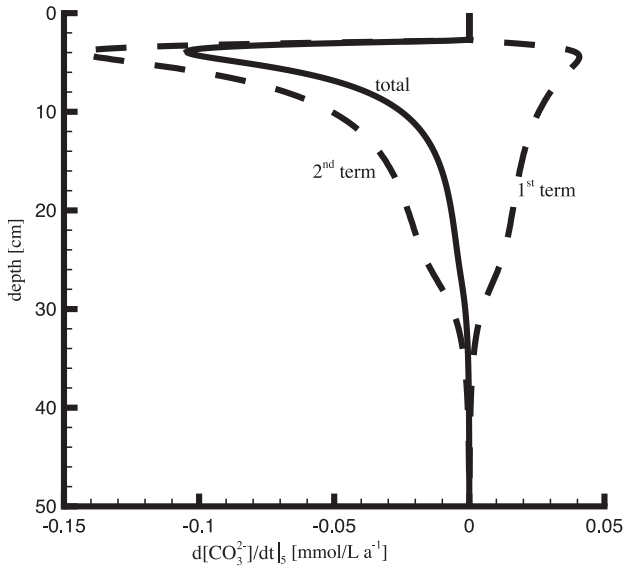

Fig. 10. Rate of change of the saturation state with respect to calcite, Ω_{17}, due to sulfate reduction (see eq 30, *Sulfur Cycling section*).

reaction network was only produced via oxidation of sulfide by MnO_2 and $Fe(OH)_3$ (reactions 12 and 13).

The predicted pH and $CaCO_3$ distributions are compared to the baseline simulation in figure 11. Pore water pH values are slightly lower due to the FeS_2 oxygenation and S^0 disproportionation reactions. Despite the minor effect on pH, there is a noticeable decrease of the $CaCO_3$ concentrations in the sediment. The enhanced $CaCO_3$ dissolution compensates for the additional proton production by FeS_2 oxygenation and S^0 disproportionation. In terms of depth-integrated rates of proton production, S^0 disproportionation and oxidation of pyrite rank only 14^{th} and 15^{th}, respectively. Compared to the baseline simulation, a major change among the sulfur bearing solids is that hardly any FeS remains (not shown). That is, reduced sulfur is now buried mainly as FeS_2 and S^0.

Calcite Dissolution

In the baseline simulation, calcite dissolution is the main sink of protons in the sediment (table 10). To further evaluate the significance of calcite dissolution, the baseline pH profile may be compared to the pH profile when calcite dissolution is completely inhibited (fig. 12). The latter is obtained by setting the calcite deposition flux, or the calcite dissolution rate constant, equal to zero. As can be seen, the absence of calcite dissolution shifts the pH profile to lower values (fig. 12, top left). The general shape of the pH profile, however, remains the same. The local pH minimum at the base of the oxygenated zone is approximately 0.2 pH units lower when no calcite dissolution takes place, relative to the baseline scenario.

Rate expressions for calcite dissolution are generally assumed to be proportional to the degree of undersaturation raised to a power n (reaction rate order) (Wollast, 1990). The constant of proportionality (k_{17} in table 9), however, is not well constrained (Jansen and others, 2002; Hales, 2003). Laboratory studies of calcite dissolution report reaction rate orders (n) ranging from 1.5 (Gledhill and Morse, 2004) to 4.5 (Keir, 1980), while n values ranging from 1 to 5 have been used in early diagenetic models of

TABLE 11

Reaction pathways, kinetic rate formulations, and related parameter values for the extended sulfur cycle (see Sulfur Cycling section)

R^{21}. pyritization
$FeS + S^0 \rightarrow FeS_2$

R^{22}. oxidative dissolution of pyrite
$2FeS_2 + 7O_2 \rightarrow \sum_{keq} s_{keq}^{22} C_{keq} + 2Fe^{2+} + 4SO_4^{2-}$

R^{23}. sulfur disproportionation
$4S^0 \rightarrow \sum_{keq} s_{keq}^{23} C_{keq} + SO_4^{2-}$

Reaction i	t_c^i	t_a^i	t_s^i
R^{21}	0	0	0
R^{22}	0	-4	0
R^{23}	0	-2	3

$$R^{21} = k_{21}[FeS][S^0](1-\phi)\rho_s$$

$$R^{22} = k_{22}[O_2][FeS_2](1-\phi)\rho_s$$

$$R^{23} = \begin{cases} 0 & \text{for } \Omega_{S^0} \equiv [H_2S] + [HS^-] \geq S_{stop} \\ k_{23}[S^0]\left(1 - \dfrac{\Omega_{S^0}}{S_{stop}}\right)(1-\phi)\rho_s & \text{for } \Omega_{S^0} < S_{stop} \end{cases}$$

Parameter Name	Parameter Value	Units	Reaction(s)
k_{21}	2.36×10^6	g mol^{-1} a^{-1}	21
k_{22}	1.51×10^4	L mol^{-1} a^{-1}	22
k_{23}	3.15×10^{-3}	a^{-1}	23
S_{stop}	10^{-5}	mol L^{-1}	23

calcite dissolution (Cai and others, 1995; Hales and Emerson, 1997b; Jahnke and others, 1997). Rate constants determined for specific sites through parameter fitting range from 0.2% day^{-1} to 1000% day^{-1} for n = 4.5, and from 4×10^{-4}% day^{-1} to 0.01% day^{-1} for n = 1. To test the response of the pH profile to calcite dissolution kinetics, we considered two additional scenarios: one with n = 4.5 and k_{17} = 1000% day^{-1}, and the other with n = 1 and k_{17} = 0.01% day^{-1}.

Over the entire depth interval considered (0–25 cm), the pore waters are in disequilibrium with respect to calcite, with supersaturation prevailing in the uppermost centimeter and undersaturation below (fig. 8). Changes in the rate constant of calcite dissolution or the reaction order, while affecting the absolute pH values, do not modify the general features of the pH profiles (fig. 12). Thus, the shape of the pH

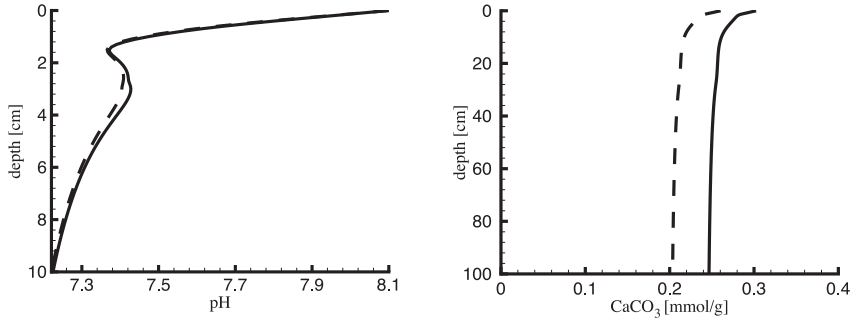

Fig. 11. Effect of sulfur cycling on pore water pH and $CaCO_3$ distributions. The solid line indicates the results of the baseline scenario, while the broken lines correspond to the additional simulation with the extended sulfur reaction network. See text for full details.

profile primarily reflects the depth distributions of the main redox reactions that consume or produce protons. The value of the local pH minimum at the base of the oxic zone, however, is quite sensitive to the dissolution kinetics of calcite. Similarly, the preservation of $CaCO_3$ in the sediment depends on the rate expression and rate constant describing calcite dissolution. Whereas 18 percent of the input flux of calcite is buried in the baseline simulation, this value increases to 39 percent for n = 1 and k_{17} = 0.01% day^{-1}, and nearly all calcite is dissolved for n = 4.5 and k_{17} = 1000% day^{-1}.

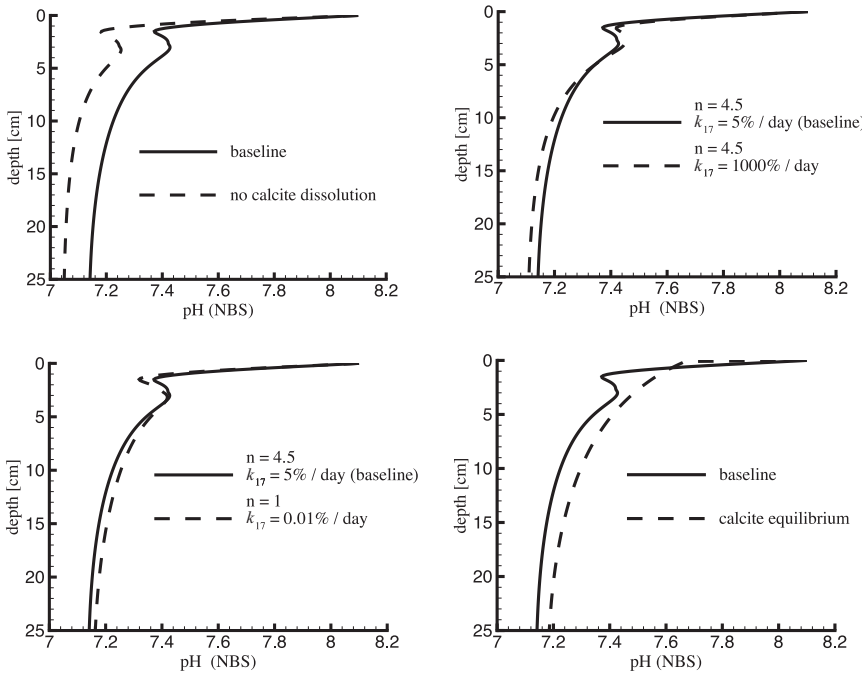

Fig. 12. Effect of calcite dissolution on pore water pH distributions. The solid line indicates the baseline scenario in all figures, while the broken lines are used for the additional simulations: no calcite dissolution (top left); increased rate constant (top right); first order reaction rate (bottom left); and calcite equilibrium (bottom right).

A very different shape of the pH profile is obtained when the pore waters are assumed to remain at equilibrium with respect to calcite, at all depths (fig. 12, bottom right). (The implementation of the calcite-pore solution equilibrium condition in the mixed kinetic-equilibrium reaction system is detailed in Appendix III). The most pronounced difference with the kinetic dissolution formulations is the disappearance of the local minimum and maximum in the pH profile (fig. 12, bottom right). The large effect of the equilibrium assumption can also be seen in the significant attenuation of the net proton production and consumption rate (fig. 9, broken lines). The pore water calcium profile is also affected (not shown), as $CaCO_3$ is now allowed to precipitate in the supersaturated upper 0.2 cm of the sediment.

The precipitation of other carbonate and sulfide minerals ($MnCO_3$, $FeCO_3$, and FeS) is also affected by the increased pH buffering effect of calcite in the equilibrium scenario (not shown). The zone of $MnCO_3$ precipitation extends to the SWI, but results in only 1.1 percent greater burial of this mineral, and a 3.3 percent decrease in the pore water Mn^{2+} concentrations at depth. The effect on the Fe cycle is far less significant as the burial of iron sulfide remains unchanged and the pore waters remain undersaturated with respect to $FeCO_3$.

Irrigation

The pore water chemistry and reaction dynamics of marine sediments deposited under oxygenated bottom waters are strongly affected by the activity of benthic macrofauna (for comprehensive reviews, see, Berner, 1980; Van Cappellen and Gaillard, 1996; Boudreau, 1997; Aller, 2001). In particular, pore water irrigation by burrowing organisms increases the fluxes of dissolved oxidants into the sediment, thereby modifying the relative importance and depth distribution of the various redox reaction pathways. Given the crucial importance of redox reactions for the production and consumption of protons, irrigation is expected to have a major influence on the pore water pH distribution.

A number of simple irrigation scenarios are investigated (fig. 13). First, we consider a 30 cm deep uniformly irrigated layer, overlying non-irrigated sediment. That is, the imposed irrigation coefficient distribution ($\alpha_k = \alpha(x)$ for all dissolved species k in equation 1) is a step function, characterized by a constant value, α_0, in depth interval 0 to 30 cm. The values of α_0 tested (2.5, 5 and 7.5 a^{-1}) are typical for mid-shelf depositional environments (Meile and Van Cappellen, 2003). The resulting oxygen penetration depths are 1.5, 3.4, 4.7 and 6.2 cm, for $\alpha_0 = 0$, 2.5, 5 and 7.5 a^{-1}, respectively.

As in the baseline simulation, the pH profiles in the irrigated scenarios display a pH minimum, although it is less pronounced than in the absence of irrigation. The pH minimum depth increases with increasing irrigation intensity, which reflects the increasingly deeper penetration of oxygen below the SWI. Thus, despite significant differences in solute transport regime among the different scenarios, the computed pH profiles all record the marked change in net proton production across the oxic-anoxic transition.

Irrigation greatly reduces the overall variation of pH with depth. In fact, the pH at the bottom of the irrigated zone is nearly the same in the presence of irrigation regardless of the irrigation intensity, yet it is ~0.36 pH units higher than in the absence of irrigation. The higher pH values in the irrigated scenarios also coincide with lower concentrations of reduced pore water species: for example, the concentrations of free sulfides, Mn^{2+}, Fe^{2+}, and NH_4^+ are lower by one to two orders of magnitude for the case of $\alpha_0 = 5\ a^{-1}$, relative to the baseline scenario.

To illustrate the potential effect of the functional dependence of the depth distribution of the irrigation coefficient, we also consider an exponentially decreasing $\alpha(x)$ profile (fig. 13). The depth attenuation constant is chosen such that at 30 cm

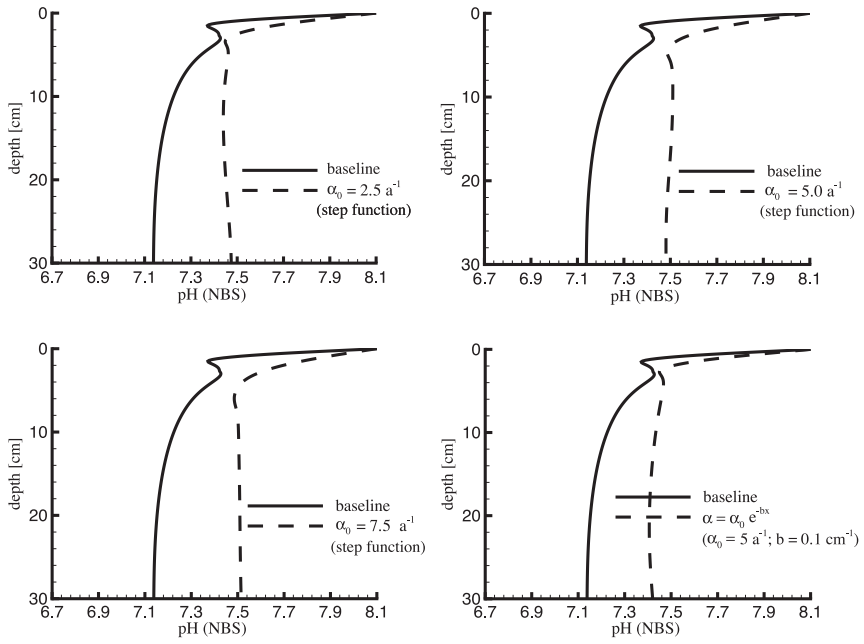

Fig. 13. Response of the pH distribution to irrigation. In the baseline scenario, there is no irrigation. In the step functions, α is set to α_0 to a depth of 30 cm and zero below.

depth α drops to 5 percent of its value at the SWI, which is set to 5 a^{-1}. The resulting pH profile is similar to that obtained using the step function depth dependence with $\alpha_0 = 2.5$ a^{-1}. The depth integrated irrigation intensity in this case (75 cm a^{-1}) most closely matches that of the exponentially decreasing $\alpha(x)$ profile (50 cm a^{-1}). This may indicate that the pH profile is more sensitive to the integrated irrigation intensity than to the exact functional depth dependence of the irrigation coefficient.

In the simulations with irrigation, it is assumed that the same irrigation coefficient $\alpha(x)$ applies to all solute species. Recent theoretical work, however, does not support this assumption but rather implies that solute-specific irrigation coefficient distributions should be assigned in reactive transport calculations (Meile and others, 2005). While this adds another level of complexity, it points to the need for early diagenetic modeling approaches that account for the individual transport properties of the various reactive species.

CONCLUSIONS

The distribution of pore water pH in aquatic sediments is controlled by a complex network of biogeochemical reaction processes. The quantitative prediction of pH profiles, therefore, requires a rigorous mathematical treatment of the coupling of acid-base equilibria, irreversible kinetic reactions and transport processes. We have addressed the specific challenges of the treatment of mixed kinetic-equilibrium reaction systems in a transport environment with solute-specific molecular diffusion coefficients. In the proposed approach the chemical species participating in equilibrium reactions appear explicitly in the kinetic reaction stoichiometries. As the stoichiometric coefficients of these species are treated as unknowns in the model, the kinetic reaction stoichiometries are allowed to vary with time and depth in the sediment.

We illustrate the general theory for deriving the stoichiometric coefficients in an example seawater, taking into account the acid-base equilibria of the dissolved inor-

ganic carbon, sulfide, and borate systems. The variable stoichiometric coefficients are expressed in terms of the stoichiometric coefficient of the proton, for which an explicit expression is derived. This method, which can be generalized to include other equilibrium reactions, yields the proton production and consumption rates due to each kinetic reaction process.

Calculation of the reaction-specific proton production and consumption rates allows us to quantitatively interpret pH distributions in aquatic sediments. The model is applied by using simulations of early diagenetic processes in a sediment representative of the continental shelf. The computed pH profiles exhibit features commonly observed in measured profiles. In particular, the occurrence of a pH minimum and maximum is explained in terms of the depth distributions of proton production and consumption by the various biogeochemical reactions. The proposed approach also provides a means to interpret the saturation state of pore waters with respect to mineral phases (carbonates, sulfides, oxides), since they are intimately linked to variations in pH. In this respect, the role of sulfate reduction in controlling the calcite saturation state is investigated, by explicitly computing the rate at which carbonate ions are produced or consumed by sulfate reduction. Model simulations are also used to determine the response of pH to variations in calcite dissolution kinetics and irrigation intensity.

The applications of the model in this study are limited to steady state simulations and they assume a constant ionic composition of the pore water. However, the proposed model approach can handle transient simulations, and account for changes in the ionic strength and relative composition of the pore water. Furthermore, the set of reaction processes considered in this study may be expanded to include additional kinetic and equilibrium reactions. The approach presented here provides a framework for the quantification of proton production and consumption rates in biogeochemical reaction-transport systems, and will hopefully enhance the utilization of the diagnostic capabilities of pH distribution in early diagenesis.

ACKNOWLEDGMENTS

We thank Ivan L'Heureux for comments on an earlier draft and Eldad Haber for useful discussions on the numerical solver. We also thank Filip Meysman and an anonymous journal reviewer for their constructive input, which helped us improve this paper. This work was financially supported by a Pioneer Programme of the Netherlands Organization for Scientific Research (NWO).

APPENDIX I

EQUILIBRIUM CONSTANTS

The coefficients, η_m in equation (11) are themselves functions of the equilibrium species concentrations and are defined as,

$$\eta_m = T_C \frac{\partial(\chi_1 + 2\chi_2)}{\partial K_m^*} + T_S \frac{\partial \sigma_1}{\partial K_m^*} + T_B \frac{\partial \beta_1}{\partial K_m^*} + \frac{\partial (K_3^*/[H^+])}{\partial K_m^*}. \tag{I-1}$$

Each apparent constant, K_m^* is a function of the activity coefficients, γ_k^* (activity coefficient of species k), which in turn depend on the total ionic strength of the solution, as well as specific interactions that may be estimated with ion pairing or Pitzer models. Expansion of the rate of change of the apparent equilibrium constants yields

$$\left.\frac{dK_m^*}{dt}\right|_i = \sum_{k=1}^{N_s} \left(\frac{\partial K_m^*}{\partial \gamma_k} \sum_{\ell=1}^{N_s} \frac{\partial \gamma_k^*}{\partial C_\ell} \left.\frac{dC_\ell}{dt}\right|_i \right), \tag{I-2}$$

where N_s is the number of species and

$$\frac{\partial K^*_m}{\partial \gamma_k} = K_m \frac{\partial}{\partial \gamma_k}\left(\prod_{\ell=1}^{N_s} \gamma_\ell^{-\nu^\ell_m}\right) = \frac{-\nu^k_m K_m}{\gamma_k}\prod_{\ell=1}^{N_s} \gamma_\ell^{-\nu^\ell_m}, \tag{I-3}$$

in which ν^k_m represents the stoichiometric coefficient of species k in the 'fast' reversible reaction, m.

The functional form of the dependence of γ^*_k on the chemical composition, that is, $\frac{\partial \gamma_k}{\partial C_\ell}$, depends on the specific ion interaction model used (see for example, Millero and Schreiber, 1982; and He and Morse, 1993). The rate of change of each species concentration can be expressed more explicitly as

$$\left.\frac{dC_\ell}{dt}\right|_i = \lambda R^i + \Lambda_0 \left.\frac{d[H^+]}{dt}\right|_i + \sum_{p=1}^{N_{eq}} \Lambda_p \left.\frac{dK^*_p}{dt}\right|_i, \tag{I-4}$$

where λ is a function of the proton concentration and the apparent equilibrium constants, and the Λ terms (Λ_0 to $\Lambda_{N_{eq}}$) are each a function of the species concentrations and apparent dissociation constants. Collectively, equations (11) and (I-2) constitute a set of coupled $N_{eq} + 1$ equations that can be solved numerically using an iterative scheme for the instantaneous rates of change of the protons and apparent dissociation constants for a given composition of the solution (that is, for known species concentrations).

Appendix II

Taylor expansion and temporal discretization

Taylor expansion of the total rate (sources and sinks) defined in equation (16) gives

$$R^j_k|_{new} \cong R^j_k|_{old} + \sum_{\ell=1}^{N_s} \left.\frac{\partial R^j_k}{\partial C^j_\ell}\right|_{old} (C^j_\ell|_{new} - C^j_\ell|_{old}), \tag{II-1}$$

where the labels *old* and *new* correspond to successive iterations. The partial differentials of total rates with respect to species concentrations are commonly represented by a Jacobian matrix. Thus, we define, at each node j, a matrix of size N_s by N_s, J^j, with elements

$$J^j(k, \ell) \equiv \frac{\partial R^j_k}{\partial C^j_\ell}. \tag{II-2}$$

The Taylor expansion allows us to linearize the set of coupled reaction-transport equations (15). At the same time, the terms involving the elements of the Jacobian matrix (eq II-1), couple the equations of all the species, and thereby require a global (or otherwise referred to as one-step) solution. Therefore, we define the vectors, $\vec{C}$ and $\vec{R}$, representing the concentrations and total rates affecting the species concentrations, for all species, k, and at all nodes, j:

$$\begin{aligned}\vec{C} &= [C^{j=1}_{k=1}, C^{j=1}_{k=2}, \cdots, C^{j=1}_{k=N_S}, C^{j=2}_{k=1}, \cdots, C^{j=2}_{k=N_S}, \cdots, C^{j=N_x}_{k=1} \cdots C^{j=N_x}_{k=N_S}] \\ \vec{R} &= [R^{j=1}_{k=1}, R^{j=1}_{k=2}, \cdots, R^{j=1}_{k=N_S}, R^{j=2}_{k=1}, \cdots, R^{j=2}_{k=N_S}, \cdots, R^{j=N_x}_{k=1} \cdots R^{j=N_x}_{k=N_S}]\end{aligned}. \tag{II-3}$$

Equation (15) can then be solved numerically by the temporal discretization at time step $m + 1$ ($t = t_{m+1}$), given the solution at time step m ($t = t_m$), and expansion of the reaction term:

$$\frac{\partial(\boldsymbol{\xi}\vec{C})}{\partial t} \approx \frac{\boldsymbol{\xi}(\vec{C}|^{t_{m+1}}_{new} - \vec{C}|^{t_m})}{\Delta t} = \boldsymbol{T}\vec{C}|^{t_{m+1}}_{new} + \vec{R}|^{t_{m+1}}_{old} + J|^{t_{m+1}}_{old}(\vec{C}|^{t_{m+1}}_{new} - \vec{C}|^{t_{m+1}}_{old}), \tag{II-4}$$

where the matrices $\boldsymbol{T}$, $\boldsymbol{\xi}$, and $\boldsymbol{J}$ are each of dimension N by N, $N = N_s N_x$, and $\Delta t = t_{m+1} - t_m$. Matrix $\boldsymbol{T}$ is a block tridiagonal matrix,

$$\boldsymbol{T} = \begin{bmatrix} [\ddots] & [\ddots] & & & \\ [\ddots] & [\ddots] & \ddots & & \\ & \ddots & \ddots & \ddots & \\ & & \ddots & [\ddots] & [\ddots] \\ & & & [\ddots] & [\ddots] \end{bmatrix}, \tag{II-5}$$

where each block is a diagonal matrix of dimension N_s by N_s. Matrix J is a block diagonal matrix,

$$J = \begin{bmatrix} [J^1] & & & & \\ & [J^2] & & & \\ & & \ddots & & \\ & & & [J^{N_x-1}] & \\ & & & & [J^{N_x}] \end{bmatrix}, \tag{II-6}$$

where the elements of the individual N_s by N_s blocks are given by equation (II-2). Matrix $\boldsymbol{\xi}$ is a diagonal matrix whose entries are the volume fractions in which the concentrations of the various species are defined at each node. The diagonal elements assume the same order as that of concentration and rate vectors (eq II-3).

Appendix III

calcite equilibrium

Equilibrium between pore water and calcite is represented by the heterogeneous equilibrium reaction

$$CaCO_{3(s)} \leftrightarrow Ca^{2+}_{(aq)} + CO^{2-}_{3(aq)}, \tag{III-1}$$

with its corresponding mass action law

$$K_{s17} = [Ca^{2+}][CO_3^{2-}], \tag{III-2}$$

where K_{s17} represents the apparent solubility constant of $CaCO_3$. The total dissolved inorganic carbon (T_C) and total alkalinity (T_A) are affected by the degree of advancement of this equilibrium reaction. Using the change in the concentration of Ca^{2+} as a measure of this advancement, the contributions to T_A and T_C are

$$\begin{aligned} \left.\frac{d(T_C)}{dt}\right|_i &= t_c^i R^i + \left.\frac{d[Ca^{2+}]}{dt}\right|_i \\ \left.\frac{d(T_A)}{dt}\right|_i &= t_a^i R^i + 2\left.\frac{d[Ca^{2+}]}{dt}\right|_i \end{aligned}, \tag{III-3}$$

which are extensions of equations (6).

The instantaneous rate of production or consumption of Ca^{2+}, $\left.\frac{d[Ca^{2+}]}{dt}\right|_i$, due to reaction R^i can be expressed in terms of the rates of proton production and T_C using the mass action law (eq III-2) and the fractions defined in equations (7) and (8)

$$\begin{aligned} \left.\frac{d[Ca^{2+}]}{dt}\right|_i &= \left.\frac{d}{dt}\left(\frac{K_{s17}}{[CO_3^{2-}]}\right)\right|_i = \frac{-K_{s17}}{[CO_3^{2-}]^2}\left.\frac{d[CO_3^{2-}]}{dt}\right|_i \\ \left.\frac{d[Ca^{2+}]}{dt}\right|_i &= \frac{-K_{s17}}{[CO_3^{2-}]^2}\left(\chi_2\left.\frac{dT_C}{dt}\right|_i + T_C\frac{\partial\chi_2}{\partial[H^+]}\left.\frac{d[H^+]}{dt}\right|_i\right) \end{aligned}. \tag{III-4}$$

Substituting the instantaneous rate of T_C (III-3) into (III-4) yields an expression for the instantaneous rate of protons production/consumption in terms of the rate of change in Ca^{2+}

$$\begin{aligned} \left.\frac{d[Ca^{2+}]}{dt}\right|_i &= \frac{-K_s}{[CO_3^{2-}]^2}\left(\chi_2\left(t_c^i R^i + \left.\frac{d[Ca^{2+}]}{dt}\right|_i\right) + T_C\frac{\partial\chi_2}{\partial[H^+]}\left.\frac{d[H^+]}{dt}\right|_i\right) \\ \left.\frac{d[H^+]}{dt}\right|_i &= \frac{P_1}{P_2}\left.\frac{d[Ca^{2+}]}{dt}\right|_i - \frac{P_3 R_i}{P_2} \end{aligned}, \tag{III-5}$$

where P_1, P_2, and P_3 are defined as

$$\begin{aligned} P_1 &\equiv 1 + \frac{K_{s17}\chi_2}{[CO_3^{2-}]^2} \\ P_2 &\equiv \frac{-K_{s17}}{[CO_3^{2-}]^2}\frac{\partial\chi_2}{\partial[H^+]}T_C. \end{aligned} \tag{III-6}$$

$$P_3 \equiv \frac{-K_{s17}}{[CO_3^{2-}]^2}\, t_c^i \chi_2$$

Expanding the total alkalinity equation and its instantaneous rate of production (eqs 9 and 10), neglecting changes of apparent equilibrium constants, yields

$$\left.\frac{dT_A}{dt}\right|_i = \left.\frac{dT_C}{dt}\right|_i (\chi_1 + 2\chi_2) + T_C \frac{\partial(\chi_1 + 2\chi_2)}{\partial[H^+]} \left.\frac{d[H^+]}{dt}\right|_i + \left.\frac{dT_S}{dt}\right|_i \sigma_1 + T_S \frac{\partial \sigma_1}{\partial[H^+]} \left.\frac{d[H^+]}{dt}\right|_i + \left.\frac{dT_B}{dt}\right|_i \beta_1 + T_B \frac{\partial \beta_1}{\partial[H^+]} \left.\frac{d[H^+]}{dt}\right|_i - \left.\frac{K_3^*}{[H^+]^2} \frac{d[H^+]}{dt}\right|_i - \left.\frac{d[H^+]}{dt}\right|_i, \quad \text{(III-7)}$$

Similarly, substituting the instantaneous rates of both T_A and T_C (eqs III-3) into equation (III-7) yields

$$t_a^i R^i + 2 \left.\frac{d[Ca^{2+}]}{dt}\right|_i = \left(t_c^i R^i + \left.\frac{d[Ca^{2+}]}{dt}\right|_i \right)(\chi_1 + 2\chi_2) + t_s^i \sigma_1 R^i + P_4 \left.\frac{d[H^+]}{dt}\right|_i, \quad \text{(III-8)}$$

where P_4 is defined as

$$P_4 \equiv T_C \frac{\partial \chi_1}{\partial[H^+]} + 2T_C \frac{\partial \chi_2}{\partial[H^+]} + T_S \frac{\partial \sigma_1}{\partial[H^+]} + T_B \frac{\partial \beta_1}{\partial[H^+]} - \frac{K_w}{[H^+]^2} - 1. \quad \text{(III-9)}$$

Substituting the proton rate (eq III-5) into equation (III-8) and solving for the calcium ion rate, we obtain

$$\left.\frac{d[Ca^{2+}]}{dt}\right|_i = \frac{(t_c^i(\chi_1 + 2\chi_2) + t_s^i \sigma_1 - t_w^i)P_2 - P_3 P_4}{(2 - \chi_1 - 2\chi_2)P_2 - P_1 P_4} R^i. \quad \text{(III-10)}$$

The above expression provides us with the stoichiometric coefficient for Ca^{2+} for each reaction i and can be substituted back into equation (III-5) for the proton rate.

References

Adler, M., Hensen, C., Wenzhöfer, F., Pfeifer, K., and Schulz, H. D., 2001, Modeling of calcite dissolution by oxic respiration in supralysoclinal deep-sea sediments: Marine Geology, v. 177, p. 167–189.

Aguilera, D. R., Jourabchi, P., Spiteri, C., and Regnier, P., 2005, A knowledge-based reactive transport approach for the simulation of biogeochemical dynamics in Earth systems: Geochemistry, Geophysics, Geosystems, v. 6, doi: 10.1029/2004GC000899.

Aller, R. C., 2001, Transport and reactions in the bioirrigated zone, *in* Boudreau, B. P., and Jorgensen, B. B., editors, The Benthic Boundary Layer: Transport processes and biogeochemistry: Oxford, Oxford Press, p. 269–301.

Archer, D., Emerson, S., and Reimers, C., 1989, Dissolution of calcite in deep-sea sediments: pH and O_2 microelectrode results: Geochimica et Cosmochimica Acta, v. 53, p. 2831–2845.

Archer, D. E., Morford, J. L., and Emerson, S. R., 2002, A model of suboxic sedimentary diagenesis suitable for automatic tuning and gridded global domains: Global Biogeochemical Cycles, v. 16, doi: 10.1029/2000GB1288.

Ben-Yaakov, S., 1973, pH buffering of pore water of recent anoxic marine sediments: Limnology and Oceanography, v. 18, p. 86–94.

Berg, P., Rysgaard, S., and Thamdrup, B., 2003, Dynamic modeling of early diagenesis and nutrient cycling. A case study in an Arctic marine sediment: American Journal of Science, v. 303, p. 905–955.

Berner, R. A., 1980, Early diagenesis: a theoretical approach: Princeton, Princeton University Press, 256 p.

Boudreau, B. P., 1986, Mathematics of tracer mixing in sediments: I. spatially-dependent, diffusive mixing: American Journal of Science, v. 286, p. 161–198.

Boudreau, B. P., 1991, Modelling the sulfide-oxygen reaction and associated pH gradients in porewaters: Geochimica et Cosmochimica Acta, v. 55, p. 145–159.

——— 1996, A method-of-lines code for carbon and nutrient diagenesis in aquatic sediments: Computers and Geosciences, v. 22, p. 479–496.

——— 1997, Diagenetic models and their implementation: Modelling transport and reactions in aquatic sediments: Berlin, Springer-Verlag, 414 p.

Boudreau, B. P., and Canfield, D. E., 1988, A provisional diagenetic model for pH in anoxic porewaters: Application to the FOAM site: Journal of Marine Research, v. 46, p. 429–455.

——— 1993, A comparison of closed- and open-system models for porewater pH and calcite-saturation state: Geochimica et Cosmochimica Acta, v. 57, p. 317–334.

Cai, W. J., and Reimers, C. E., 1993, The development of pH and P_{CO2} microelectrodes for studying the carbonate chemistry of pore waters near the sediment-water interface: Limnology and Oceanography, v. 38, p. 1762–1773.

Cai, W. J., Reimers, C. E., and Shaw, T., 1995, Microelectrode studies of organic carbon degradation and calcite dissolution at a California Continental rise site: Geochimica et Cosmochimica Acta, v. 59, p. 497–511.

Cai, W. J., Zhao, P., and Wang, Y., 2000, pH and pCO_2 microelectrode measurements and the diffusive behavior of carbon dioxide species in coastal marine sediments: Marine Chemistry, v. 70, p. 133–148.

Carman, R., and Rahm, L., 1997, Early diagenesis and chemical characteristics of interstitial water sediments in the deep deposition bottoms of the Baltic proper: Journal of Sea Research, v. 37, p. 25–47.

Chester, R., 2000, Marine Geochemistry: Oxford, Blackwell Science, 506 p.

Cussler, E. L., 1984, Diffusion: Mass transfer in fluid systems: New York, Cambridge University Press, 525 p.

Fisher, J. B., and Matisoff, G., 1981, High resolution vertical profiles of pH in recent sediments: Hydrobiologia, v. 79, p. 277–284.

Forja, J. M., Ortega, T., DelValls, T. A., and Gómez-Parra, A., 2004, Benthic fluxes of inorganic carbon in shallow coastal ecosystems of the Iberian Peninsula: Marine Chemistry, v. 85, p. 141–156.

Gaillard, J. F., Pauwels, H., and Michard, G., 1989, Chemical diagenesis in coastal marine sediments: Oceanologica Acta, v. 12, p. 175–187.

Gledhill, D. K., and Morse, J. W., 2004, Dissolution kinetics of calcite in NaCl-$CaCl_2$-$MgCl_2$ brines at 25°C and 1 bar pCO_2: Aquatic Geochemistry, v. 10, p. 171–190.

Hales, B., 2003, Respiration, dissolution, and the lysocline: Paleoceanography, v. 18, doi: 10.1029/2003PA000915.

Hales, B., and Emerson, S., 1996, Calcite dissolution in sediments of the Ontong-Java Plateau: *in situ* measurements of pore water O_2 and pH: Global Biogeochemical Cycles, v. 10, p. 527–541.

——— 1997a, Calcite dissolution in sediments of the Ceara Rise: *In situ* measurements of porewater O_2, pH, and $CO_{2(aq)}$: Geochimica et Cosmochimica Acta, v. 61, p. 501–514.

——— 1997b, Evidence in support of first-order dissolution kinetics of calcite in seawater: Earth and Planetary Science Letters, v. 148, p. 317–327.

Hales, B., Emerson, S., and Archer, D., 1994, Respiration and dissolution in the sediments of the western North Atlantic: Estimates from models of *in situ* microelectrode measurements of porewater oxygen and pH: Deep-Sea Research II, v. 41, p. 695–719.

He, S. L., and Morse, J. W., 1993, The carbonic-acid system and calcite solubility in aqueous Na-K-Ca-Mg-Cl-SO_4 solutions from 0 to 90°C: Geochimica et Cosmochimica Acta, v. 57, p. 3533–3554.

Hensen, C., Landenberger, H., Zabel, M., Gundersen, J. K., Glud, R. N., and Schulz, H. D., 1997, Simulation of early diagenetic processes in continental slope sediments off southwest Africa: The computer model CoTAM tested: Marine Geology, v. 144, p. 191–210.

Iversen, N., and Jørgensen, B. B., 1993, Diffusion coefficients of sulfate and methane in marine sediments: Influence of porosity: Geochimica et Cosmochimica Acta, v. 57, p. 571–578.

Jahnke, R. A., Craven, D. B., McCorkle, D. C., and Reimers, C. E., 1997, $CaCO_3$ dissolution in California continental margin sediments: The influence of organic matter remineralization: Geochimica et Cosmochimica Acta, v. 61, p. 3587–3604.

Jansen, H., Wolf-Gladrow, D. A., and Zeebe, R. E., 2002, Modeling the dissolution of settling $CaCO_3$ in the ocean: Global Biogeochemical Cycles, v. 16, doi: 10.1029/2000GB001279.

Keir, R. S., 1980, The dissolution kinetics of biogenic calcium carbonates in seawater: Geochimica et Cosmochimica Acta, v. 44, p. 241–252.

Komada, T., Reimers, C. E., and Boehme, S. E., 1998, Dissolved inorganic carbon profiles and fluxes determined using pH and P_{CO2} microelectrodes: Limnology and Oceanography: v. 43, p. 769–781.

Kulik, D. A., Kersten, M., Heiser, U., and Neumann, T., 2000, Application of Gibbs energy minimization to model early-diagenetic solid-solution aqueous-solution equilibria involving authigenic rhodochrosites in anoxic Baltic Sea sediments: Aquatic Geochemistry, v. 6, p. 147–199.

Lerman, A., 1979, Geochemical processes: Water and sediment environments: New York, John Wiley and Sons, 481 p.

Li, Y. H., and Gregory, S., 1974, Diffusion of ions in sea water and in deep-sea sediments: Geochimica et Cosmochimica Acta, v. 38, p. 703–714.

Luff, R., and Wallmann, K., 2003, Fluid flow, methane fluxes, carbonate precipitation and biogeochemical turnover in gas hydrate-bearing sediments at Hydrate Ridge, Cascadia Margin: Numerical modeling and mass balance: Geochimica et Cosmochimica Acta, v. 67, p. 3403–3421.

Luff, R., Walmann, K., Grandel, S., and Schlüter, M., 2000, Numerical modeling of benthic processes in the deep Arabian Sea: Deep-Sea Research II, v. 47, p. 3039–3072.

Luff, R., Haeckel, M., and Wallmann, K., 2001, Robust and fast FORTRAN and MATLAB® libraries to calculate pH distributions in marine systems: Computers and Geosciences, v. 27, p. 157–169.

Mackenzie, F. T., Vink, S., Wollast, R., and Chou, L., 1995, Comparative geochemistry of marine saline lakes, *in* Lerman, A., Imboden, D., and Gat, J., editors, Physics and Chemistry of Lakes: Berlin, New York, Springer-Verlag, p. 265–278.

Marzal, P., Seco, A., Ferrer, J., and Gabaldón, C., 1994, Modeling multiple reactive solute transport with adsorption under equilibrium and nonequilibrium conditions: Advances in Water Resources, v. 17, p. 363–374.

Meile, C., and Van Cappellen, P., 2003, Global estimates of enhanced solute transport in marine sediments: Limnology and Oceanography, v. 48, p. 777–786.

Meile, C., Berg, P., Van Cappellen, P., and Tuncay, K., 2005, Solute-specific pore water irrigation: Implications for chemical cycling in early diagenesis: Journal of Marine Research, v. 63, p. 601–621.

Meysman, F. J. R., Middelburg, J. J., Herman, P. M. J., and Heip, C. H. R., 2003, Reactive transport in surface sediments. I. Model complexity and software quality: Computers and Geosciences, v. 29, p. 291–300.
Middelburg, J. J., de Lange, G. J., and Kreulen, R., 1990, Dolomite formation in anoxic sediments of Kau Bay, Indonesia: Geology, v. 18, p. 399–402.
Millero, F. J., and Schreiber, D. R., 1982, Use of the ion pairing model to estimate the activity coefficients of the ionic components of natural waters: American Journal of Science, v. 282, p. 1508–1540.
Millero, F. J., and Sohn, M. L., 1992, Chemical Oceanography: Boca Raton, CRC Press, 531 p.
Morel, F. M. M., and Hering, J. G., 1993, Principles and applications of aquatic chemistry: New York, Wiley, 588 p.
Mucci, A., Sundby, B., Gehlen, M., Arakaki, T., Zhong, S., and Silverberg, N., 2000, The fate of carbon in continental shelf sediments of eastern Canada: a case study: Deep-Sea Research II, v. 47, p. 733–760.
Müller, B., Wang, Y., Dittrich, M., and Wehrli, B., 2003, Influence of organic carbon decomposition on calcite dissolution in surficial sediments of a freshwater lake: Water Research, v. 37, p. 4524–4532.
Mulsow, S., Boudreau, B. P., and Smith, J. N., 1998, Bioturbation and porosity gradients: Limnology and Oceanography, v. 43, p. 1–9.
Pilson, M. E. Q., 1998, An introduction to the chemistry of the sea: Upper Saddle River, Prentice-Hall, 431 p.
Regnier, P., O'Kane, J. P., Steefel, C. I., and Vanderborght, J. P., 2002, Modelling complex multi-component reactive-transport systems: Towards a simulation environment based on the concept of a Knowledge Base: Applied Mathematical Modelling, v. 26, p. 913–927.
Reimers, C. E., Ruttenberg, K. C., Canfield, D. E., and Christiansen, M. B., 1996, Porewater pH and authigenic phases formed in the uppermost sediments of the Santa Barbara Basin: Geochimica et Cosmochimica Acta, v. 60, p. 4037–4057.
Stumm, W., and Morgan, J. J., 1996, Aquatic chemistry: Chemical equilibria and rates in natural waters: New York, Wiley Interscience, 1022 p.
Thamdrup, B., Rossello-Mora, R., and Amann, R., 2000, Microbial manganese and sulfate reduction in Black Sea shelf sediments: Applied and Environmental Microbiology, v. 66, p. 2888–2897.
Tsunogai, S., and Noriki, S., 1991, Particulate fluxes of carbonate and organic carbon in the ocean. Is the marine biological activity working as a sink of the atmospheric carbon?: Tellus, v. 43B, p. 256–266.
Van Cappellen, P., and Gaillard, J. F., 1996, Biogeochemical dynamics in aquatic sediments, *in* Lichtner, E. A., Steefel, C. I., and Oelkers, E., editors, Reactive transport in porous media: Mineralogical Society of America, Reviews in Mineralogy, v. 34, p. 335–376.
Van Cappellen, P., and Wang, Y., 1995, Metal cycling in surface sediments: Modeling the interplay of transport and reaction, *in* Allen, H. E., editor, Metal contaminated sediments: Chelsea, Ann Arbor Press, p. 21–62.
——— 1996, Cycling of iron and manganese in surface sediments: A general theory for the coupled transport and reaction of carbon, oxygen, nitrogen, sulfur, iron, and manganese: American Journal of Science, v. 296, p. 197–243.
Wang, Y., and Van Cappellen, P., 1996, A multicomponent reactive transport model of early diagenesis: P., Application to redox cycling in coastal marine sediments: Geochimica et Cosmochimica Acta, v. 60, p. 2993–3014.
Wenzhöfer, F., Adler, M., Kohls, O., Hensen, C., Strotmann, B., Boehme, S., and Schulz, H. D., 2001, Calcite dissolution driven by benthic mineralization in the deep-sea: *In situ* measurements of Ca^{2+}, pH, pCO_2, and O_2: Geochimica et Cosmochimica Acta, v. 65, p. 2677–2690.
Wijsman, J. W. M., Herman, P. M. J., Middelburg, J. J., and Soetaert, K., 2002, A model for early diagenetic processes in sediments of the continental shelf of the Black Sea: Estuarine, Coastal and Shelf Science, v. 54, p. 403–421.
Wollast, R., 1990, Rate and mechanism of dissolution of carbonates in the system $CaCO_3$-$MgCO_3$, *in* Stumm, W., editor, Aquatic chemical kinetics: reaction rates of processes in natural waters: New York, Wiley, p. 431–445.
Wollast, R., and Vanderborght, J. P., 1994, Aquatic carbonate systems: chemical processes in natural waters and global cycles, *in* Bidoglio, G., and Stumm, W., editors, Chemistry of Aquatic Systems: Local and Global Perspectives: Chemical and Environmental Sciences, v. 5, p. 47–71.